



Mapping ultramafic cumulates at the Tulameen ultramafic-mafic Alaskan-type intrusion, south-central British Columbia, aided by remotely piloted aircraft system photogrammetry

Dylan W. Spence^{1, a}, Henry Crawford², James S. Scoates¹, James A. Nott¹, Graham T. Nixon³, and Dejan Milidragovic^{3, 4}

¹ Pacific Centre for Isotopic and Geochemical Research, Department of Earth, Ocean and Atmospheric Sciences, University of British Columbia, Vancouver, BC, V6T 1Z4

² Department of Earth, Ocean and Atmospheric Sciences, University of British Columbia, Vancouver, BC, V6T 1Z4

³ British Columbia Geological Survey, Ministry of Energy, Mines and Low Carbon Innovation, Victoria, BC, V8W 9N3

⁴ Geological Survey of Canada, Vancouver, BC, V6B 5J3

^a corresponding author: dspence@eoas.ubc.ca

Recommended citation: Spence, D.W., Crawford, H., Scoates, J.S., Nott, J.A., Nixon, G.T., and Milidragovic, D., 2022. Mapping ultramafic cumulates at the Tulameen ultramafic-mafic Alaskan-type intrusion, south-central British Columbia, aided by remotely piloted aircraft system photogrammetry. In: Geological Fieldwork 2021, British Columbia Ministry of Energy, Mines and Low Carbon Innovation, British Columbia Geological Survey Paper 2022-01, pp. 103-122.

Abstract

The Tulameen intrusion (Late Triassic), an 18 by 6 km ultramafic-mafic body in the Quesnel terrane of southern British Columbia, is hosted by metavolcanic and metasedimentary rocks of the Nicola Group (Upper Triassic). The intrusion is zoned, with a dunite core passing outwards through olivine clinopyroxenite and clinopyroxenite, to hornblende clinopyroxenite and hornblendite at the margin. It contains widespread gabbroic rocks and a dioritic-syenodioritic phase along the southeastern margin. Detailed mapping along a >4 km transect of near-continuous exposure in the Tulameen River during a period of low water level was assisted by a remotely piloted aircraft system (RPAS). Overlapping, high-resolution digital imagery acquired by the RPAS was used to create 3-dimensional (3D) models, digital elevation models, and orthomosaics using Structure-from-Motion (SfM) photogrammetry. The transect along the Tulameen River includes dunite, chromitite, olivine clinopyroxenite, hornblende clinopyroxenite, gabbro, and minor olivine wehrlite. These rocks are cut by layered gabbro-diorite tabular bodies and fine-grained mafic to intermediate dikes. Contacts between the major map units are predominantly north-trending shear zones. Primary intrusive contacts are rarely exposed, and are typically limited to olivine clinopyroxenite, hornblende clinopyroxenite, and gabbro. Zones of intermingled ultramafic cumulates defined by entrained and variably deformed enclaves of dunite and olivine wehrlite in olivine clinopyroxenite are typical of the section. These zones are interpreted to record magma recharge and remobilization of crystal-rich magma mushes across a range of physical and rheological conditions.

Keywords: Alaskan-type, ultramafic-mafic intrusion, Tulameen intrusion, remotely piloted aircraft system (RPAS), photogrammetry, dunite, olivine clinopyroxenite

1. Introduction

The products of subduction zone magmatism include diverse volcanic and plutonic rocks. Alaskan-type, or Ural-Alaskan-type, ultramafic-mafic intrusions, such as the Tulameen intrusion (Late Triassic) in southern British Columbia (Fig. 1), are volumetrically minor, yet petrologically important, members of subduction zone magmatism (Findlay, 1969; Irvine, 1974; Nixon et al., 1997). These ultramafic-mafic rocks, characterized by a lack of orthopyroxene (Fig. 2), are cumulates that form by segregation and accumulation of crystals in a magma chamber. The Tulameen Alaskan-type intrusion is zoned (Fig. 3), with a dunite core passing outwards through olivine clinopyroxenite to hornblende clinopyroxenite and hornblendite at the margin (Findlay, 1963, 1969). Gabbroic rocks are concentrated in the eastern, central, and south-central

parts of the intrusion, and a voluminous dioritic-syenodioritic phase occupies the southeastern margin (Fig. 3). Convergent margin-related ultramafic-mafic intrusions in British Columbia are known for magmatic Ni-Cu-PGE mineralization (Scheel et al., 2009; Nixon et al., 2015; Manor et al., 2016, 2017; Jackson-Brown, 2017; Nixon et al., 2020). The emplacement and crystallization of the Tulameen intrusion, which contains newly discovered magmatic copper sulphide mineralization in the Champion zone (Nixon et al., 2020), coincides with the most prolific time of copper-gold porphyry mineralization in British Columbia (Logan and Mihalynuk, 2014).

Many plutonic rocks in the middle to upper crust are formed through the incremental emplacement and amalgamation of smaller volume magma batches (e.g., Matzel et al., 2006; Schoene et al., 2012; Annen et al., 2015; Mungall et al., 2016;

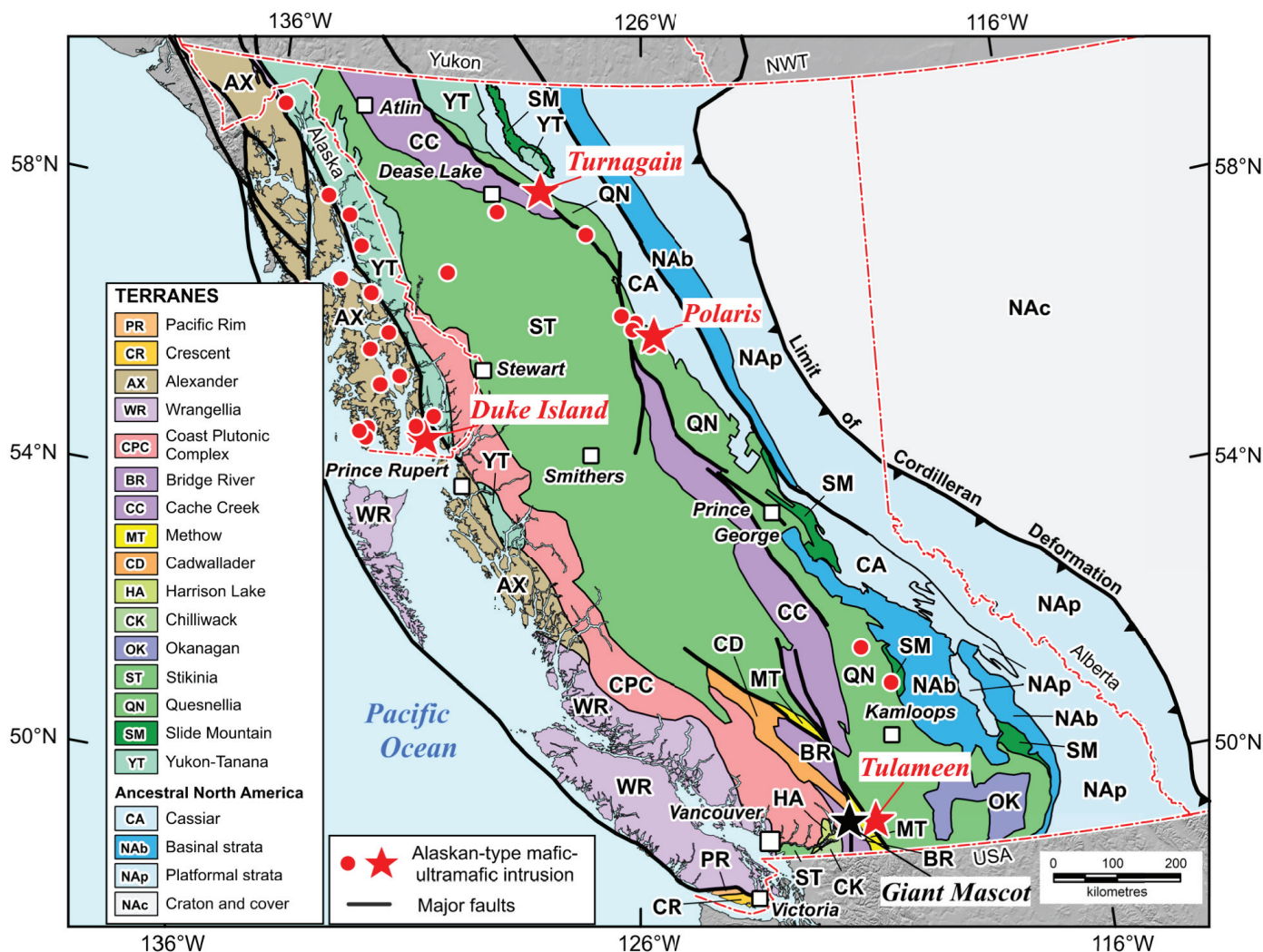


Fig. 1. Terrane map of British Columbia and southeastern Alaska (after Colpron and Nelson, 2011) showing the distribution of Alaskan-type ultramafic-mafic intrusions (after Himmelberg and Loney, 1995; Nixon et al., 1997). The Tulameen, Polaris, Turnagain, and Duke Island Alaskan-type intrusions are highlighted by red-filled stars and all other Alaskan-type intrusions are shown as red-filled circles. The Giant Mascot (Late Cretaceous) orthopyroxene-bearing intrusion and associated Ni-Cu-PGE deposit is shown for reference; black-filled star (Manor et al., 2016, 2017).

Wall et al., 2018; Yao et al., 2021; Scoates et al., 2021). Diverse textural and mineralogical features in individual intrusive bodies, which have been attributed to crystal-rich magma mixing, has garnered attention in felsic plutonic systems (e.g., Paterson, 2009; Weinberg et al., 2021), and mixing of crystal-rich magmas has been explored through numerical simulations in mafic plutonic systems (Bergantz et al., 2015; Schleicher et al., 2016). However, with the notable exception of work by Nixon et al. (2020), who recognized the effects of remobilized ultramafic cumulates in the Tulameen intrusion, and Nott et al. (2020a, 2020b), who gave detailed descriptions providing evidence for local disaggregation and remobilization of semi-consolidated ultramafic cumulates at the Polaris Alaskan-type intrusion, there has been little direct application to mafic intrusions in the rock record.

The Tulameen Alaskan-type intrusion contains a sequence along the Tulameen River of predominantly olivine

clinopyroxenite with entrained and deformed blocks of dunite and wehrlite. This chaotic association of cumulates was interpreted as a ‘syn-magmatic avalanche deposit’ (Nixon et al., 2020). Because of good access and excellent exposure, the Tulameen River is an ideal setting to investigate mixing of crystal-rich mafic magmas. In the summer of 2021, during a period of exceptionally low water levels, we carried out detailed mapping and sampling of ultramafic rocks exposed along the Tulameen River. We augmented traditional field mapping by using a remotely piloted aircraft system (RPAS) with an onboard digital RGB camera. Imagery of the study area was used to process 3D models, digital elevation models, and orthomosaics. In this contribution, we present the preliminary results of this mapping by describing the main rock types exposed along the Tulameen River and their interrelationships. The field site is on the traditional territories of the Nlaka’pamux and Syilx Okanagan nations.

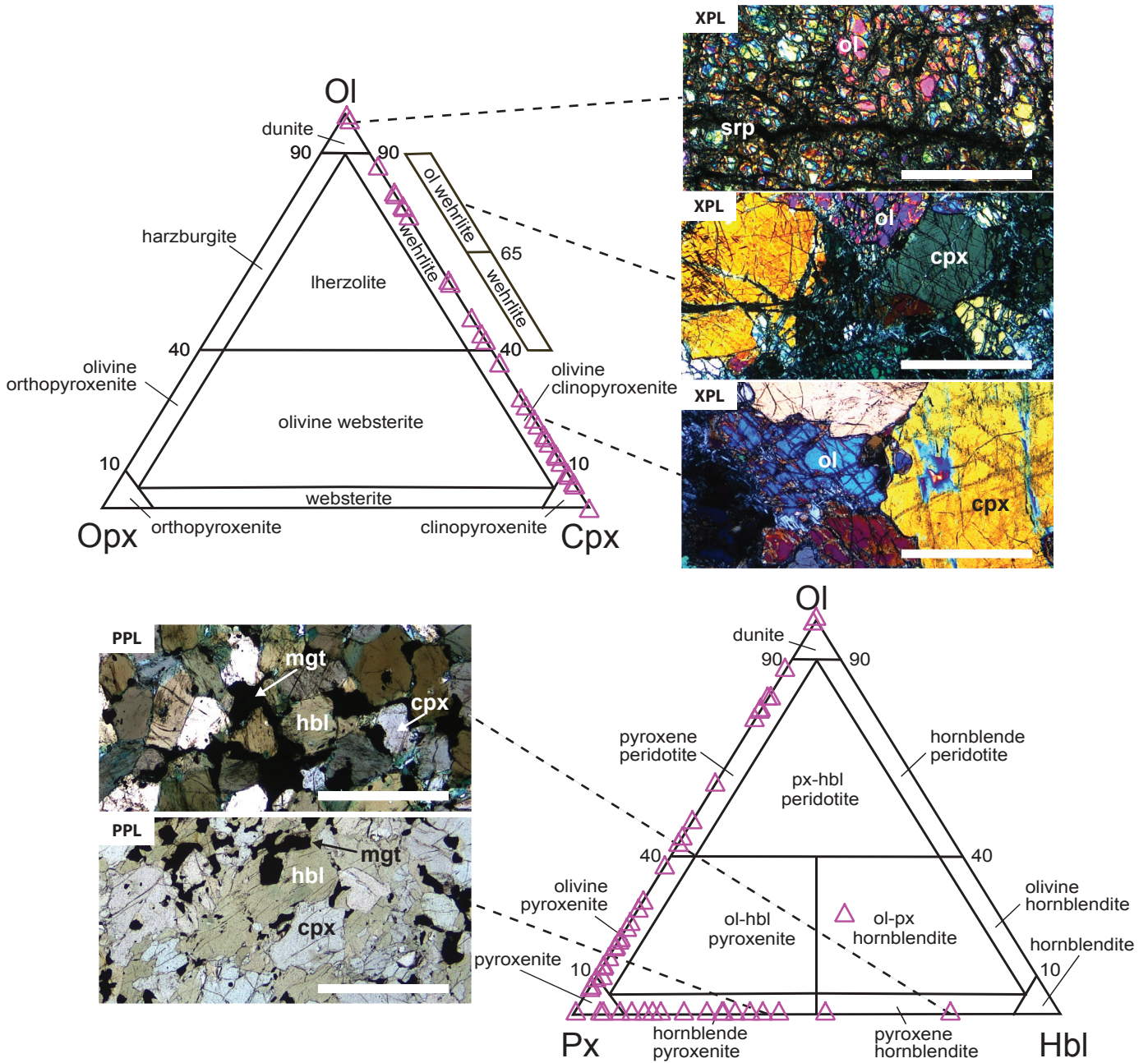


Fig. 2. IUGS ternary classification of ultramafic rocks (Le Maitre, 1989) with unofficial sub-classifications of olivine wehrlite and wehrlite and modal analyses for typical ultramafic rocks in the Tulameen intrusion (Findlay, 1963) illustrating the characteristic lack of orthopyroxene in Alaskan-type intrusions (adapted from Nixon et al., 2015). Representative photomicrographs of selected rock types from the Tulameen intrusion in cross-polarized light (XPL) or plane-polarized light (PPL). Scale bars are 1 mm. Abbreviations: cpx = clinopyroxene; hbl = hornblende; mgt = magnetite; ol = olivine; px = pyroxene; srp = serpentine.

2. Previous work

First mentioned the early 1900s (e.g., Kemp, 1902), the Tulameen intrusion is recognized as the source of platinum for nearby placer deposits. Comprehensive geology and economic mineral reports were provided by Camsell (1913) and Rice (1947). The first detailed accounts of the geology and petrology of the Tulameen intrusion were by Findlay (1963, 1969) followed by St. Louis et al. (1986), Nixon and Rublee (1988),

Nixon (1990), and Rublee (1989, 1994). The last decade has seen an increased focus on mapping convergent margin ultramafic intrusions due to their Ni-Cu-PGE mineralization potential (e.g., Manor et al., 2014; Nixon et al., 2017; Nixon, 2018; Nott et al., 2020b). The most recent map of the Tulameen Alaskan-type intrusion by Nixon (2018) modified the original mapping of Findlay (1963) and subsequent mapping by Nixon et al. (1997). Ongoing work on the Tulameen intrusion includes

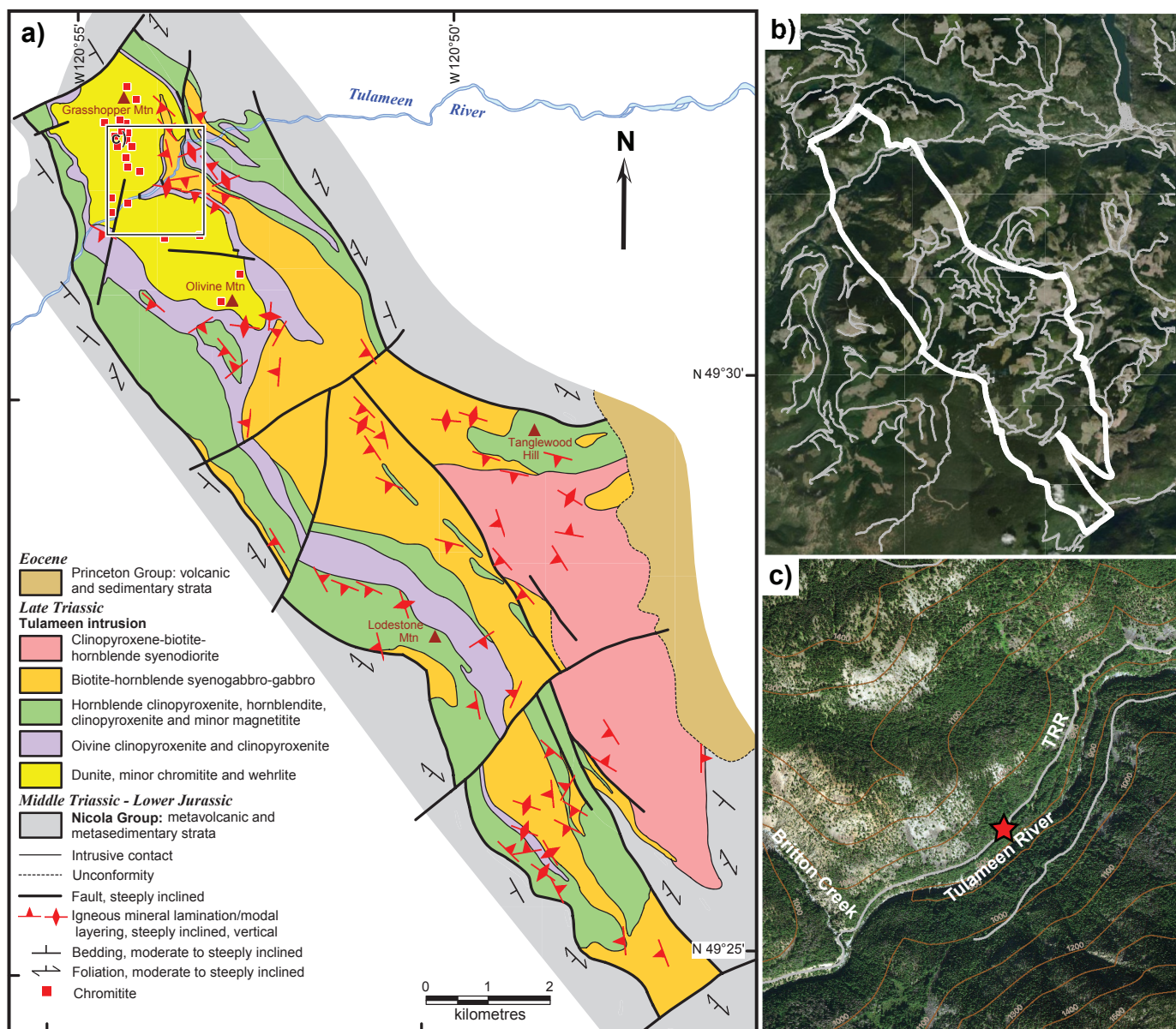


Fig. 3. Tulameen Alaskan-type intrusion. **a)** Generalized geology (Nixon et al., 1997; Nixon, 2018) illustrating lithostratigraphic units, contact relationships, and intrusive rock types. **b)** Tiled ESRI satellite image (October 15, 2018; downloaded November 7, 2021) with the outline of the Tulameen intrusion (white) and forest service roads (grey). **c)** Microsoft Bing satellite image (downloaded November 7, 2021) of the Tulameen River. Red star indicates location of parking pull-out and trail access. The Tulameen River Road (TRR) is in grey.

establishing a geochronological framework through U-Pb zircon geochronology and evaluating the extent and mineralogy of the mineralized Champion zone (e.g., Nixon et al., 2020).

3. Geological setting

The Tulameen Alaskan-type intrusion is in the Intermontane Belt of south-central British Columbia, in the southern part of the Quesnel terrane (Fig. 1). The 60 km² intrusion has a dike- or sill-like form (18 km long by 6 km maximum width) that is broadly concordant with the regional structural grain. Bedding attitudes in mafic to felsic metavolcanic and metasedimentary host rocks of the Nicola Group (Upper Triassic) strike north-

northwesterly and dip moderately to steeply to the west (Fig. 3; Nixon, 2018). Contacts with rocks of the Nicola Group are defined by shear zones (Nixon and Rublee, 1988; Rublee, 1989). The Tulameen intrusion and its Nicola Group host rocks are unconformably overlain by terrigenous siliciclastic and volcanic rocks of the Princeton Group (Eocene) to the east (Nixon, 2018). Both the Nicola Group and the Tulameen intrusion are overprinted by post-Triassic deformation and upper greenschist- to lower amphibolite-facies metamorphism. The age of the deformation and metamorphism is considered to be broadly synchronous with the intrusion of the Late Jurassic Eagle granodiorite-tonalite pluton (ca. 157-148 Ma, U-Pb

zircon; Greig et al., 1992), 1 km to the west.

Preliminary U-Pb zircon geochronology indicates emplacement and crystallization of the Tulameen intrusion during a relatively restricted time interval (204-206 Ma) in the Late Triassic (Nixon et al., 2020). This interval coincides with a 6 million-year magmatic flare-up centred on 205 Ma in the Stikine and Quesnel arcs that produced more than 90% of the known copper endowment of these two terranes (Logan and Mihalynuk, 2014). Enhanced magmatic activity at this time has been attributed to stalled subduction and arc-parallel tearing of the subducting slab that led to early (ca. 210 Ma) production of picritic magmas followed by lower degree partial melts parental to the alkalic porphyry Cu-Au deposits (Logan and Mihalynuk, 2014). The age of the Tulameen intrusion suggests a possible petrogenetic relationship between Alaskan-type ultramafic-mafic intrusions, the cumulate products of hydrous, near-primary (e.g., up to Fo_{92} olivine, Nixon et al., 1990; Rublee, 1994; Scheel, 2007; Spence, 2020), mantle-derived arc magmas, and the tectonomagmatic mechanisms that produced the Late Triassic-Early Jurassic porphyry Cu-Au deposits in the Stikine-Quesnel arc systems.

4. Remotely piloted aircraft system photogrammetry methods

4.1. Remotely piloted aircraft systems

A remotely piloted aircraft system (RPAS) assisted with mapping and spatially recording sample sites by acquiring aerial photographs. Commonly referred to as unmanned aerial vehicles (UAV), unmanned aircraft systems (UAS), or informally, drones, RPAS are defined as “a navigable aircraft, other than a balloon, rocket or kite, that is operated by a pilot who is not on board” (Transport Canada, 2021). The utility of RPAS in geological field investigations has been demonstrated in the past decade (e.g., Carrivick et al., 2013; Hansman and Ring, 2019; Elia and Ferbey, 2020). For this study, we used a DJI Mini 2 quadcopter to acquire aerial photographs obliquely and at nadir (Fig. 4). This RPAS is controlled remotely using a mobile device, running the DJI Fly app, that is plugged into a handheld controller. The 12-megapixel camera has a 1/2.3-inch CMOS sensor and a fixed 24 mm focal length lens with fixed aperture ($f/2.8$); camera orientation is manipulated using a 3-axis motorized gimbal. This RPAS is small and can easily fit into a backpack for field use and, because it is <250 g, registration with Transport Canada is not required, nor does the pilot require a Transport Canada issued RPAS licence. Because the DJI Mini 2 quadcopter does not have autopilot capabilities, the RPAS was flown manually, and photographs were captured with two-thirds overlap between adjacent photos to improve image alignment. Imagery was observed live using the DJI Fly app with a ‘rule of thirds’ grid, and the shutter was triggered using the handheld controller at optimal overlap.

4.2. Photogrammetric DEMs and orthomosaics

High-resolution RPAS-borne digital imagery can be processed into products that support geological mapping. Structure from

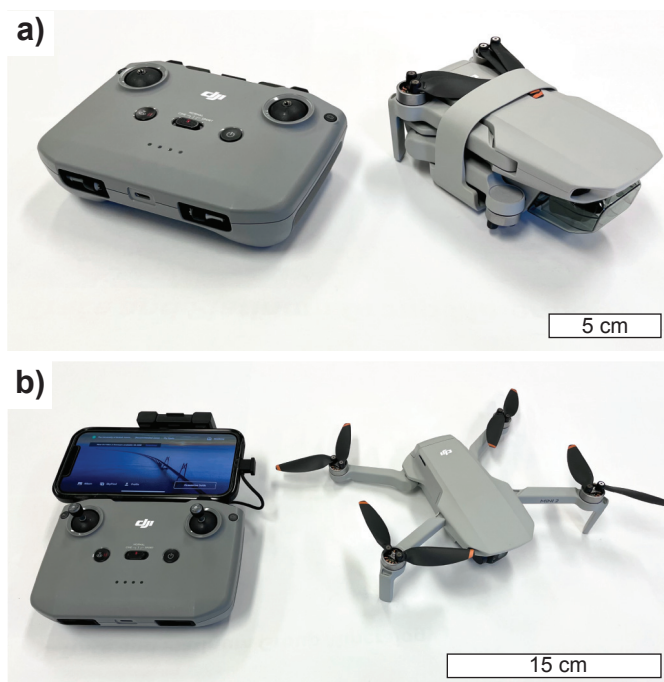


Fig. 4. Remotely piloted aircraft system (RPAS) equipment used in this study. **a)** RPAS controller and aircraft (DJI Mini 2) folded for easy transport. **b)** RPAS controller, monitor (mobile device), and unfolded aircraft ready for flight.

motion (SfM) is the photogrammetric imaging method used to generate 3D representations of scenes and objects as digital point clouds from these data. This method simultaneously resolves camera orientation and geometry by matching similar points between images of different perspectives. The ‘structure’ of a scene is derived from changes in perspective, or ‘motion’, of the camera (Shervais, 2016). The process identifies matching features, called keypoint descriptors, from overlapping photographs to generate a low-density point cloud, which is then used to establish a high-density point cloud (Carrivick et al., 2013; Shervais, 2016).

The raw SfM data are fixed in a local-coordinate plane, but when spatial controls are added to the model, these products become proportionally scaled and referenced in geographic space. Ground sampling distance (GSD), or spatial resolution, of output models is scalable because it is a product of sensor height and pixel quality (e.g., Westoby et al., 2012; Balaguer-Puig et al., 2017). This process commonly uses high-precision global positioning system (GPS) tools that use base stations like differential-GNSS, real-time kinematic (RTK) positioning, or precise point positioning to provide stable locations, known as ground control points (GCPs), in the studied area (Hansman and Ring, 2019). The RPA may have onboard RTK capability, which would reduce the need for GCPs (Elia and Ferbey, 2020).

A suite of products can be derived from generated point clouds such as 3D meshes, digital elevation models (DEMs), and orthomosaics. These digital representations, or models, have the potential to be highly accurate estimations of real-

world topography if proper data acquisition and processing steps are taken (Mosbrucker et al., 2017; James et al., 2019). This ability to quantify, manipulate, and archive features in the field, using relatively low-cost equipment, makes SfM an accessible method of 3D reconstruction (e.g., James and Robsin, 2012; Westoby et al., 2012; Eltner et al., 2016; Smith et al., 2016; Mosbrucker et al., 2017; Hansman and Ring, 2019; James et al., 2019; Elia and Ferbey, 2020).

4.3. Data acquisition and processing

Image collection and photogrammetry processing methods for acquiring semi-quantitative data can be split into four main components (Fig. 5): 1) data acquisition; 2) processing to make digital point clouds; 3) orthographic modelling to produce DEMs and orthomosaics; and 4) 3D model generation. To obtain cm-scale GSD, the drone was flown at ca.10 m above ground level (AGL). Photographs were captured at a stationary hover. GCPs were not used in this study because of trade-offs between spatial accuracy, ground resolution, and field-time, and the latter two were prioritized. Obtaining enough photographs for each GCP at low flying elevations requires greater than two-thirds overlap due to the small image footprint, making it a time- and computationally-intensive process. Furthermore, because RPAS in this study was used to record detailed lithological relationships and portray them in 3D rather than for quantitative analysis, the precision of the on-board GPS system was considered sufficient for location and scaling.

Five flights were conducted during this study, which were processed as two model groups. Flights 1, 2, and 3 prioritized a well-exposed section of bedrock mapped as olivine clinopyroxenite (Fig. 6) that was considered a ‘syn-magmatic avalanche deposit’ by Nixon et al. (2020). Flights 4 and 5 obtained imagery for the mapped contact between olivine clinopyroxenite and dunite (Fig. 6). Images were taken using consistent ISO (100 or 200) and shutter speed (1/800 or 1/1000) for each flight. Image alignment and generation of the dense point cloud were locally processed in the field using Agisoft Metashape software (version 1.7.3) on a laptop with a 2.3 GHz 8-Core Intel processor, 16 GB RAM, and an AMD Radeon Pro 5500M graphics card. Photographs were aligned using their full quality to resolve the most accurate tie points between images, whereas building of the dense point cloud was completed in ‘low’ quality because this process is computationally intensive (Table 1).

5. Photogrammetric analysis

Flights 1, 2, and 3 have an average image overlap of seven photographs per point and yielded a dense cloud of 1.38×10^7 points. A greater photo overlap for a given location typically results in a more resolved spatial model (Fig. 7a; Elia and Ferbey, 2020). The DEM produced from these flights shows relative topography at a detailed resolution of 2.79 cm/pixel (Fig. 7b). In this part of the Tulameen River, the total elevation range is approximately 14 m rising from east to west. The

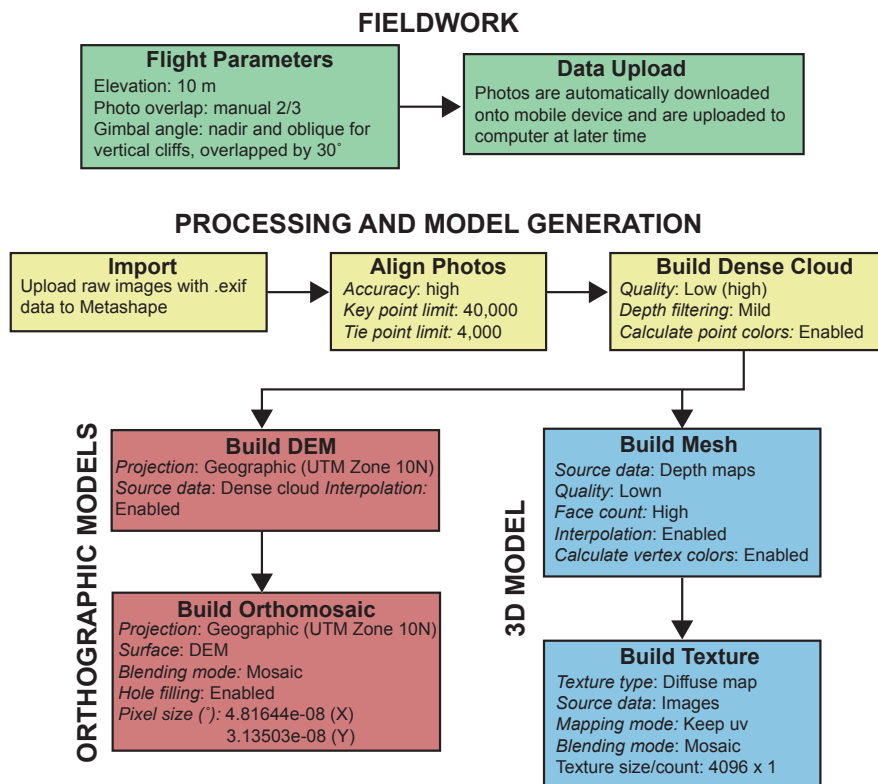


Fig. 5. Flow chart illustrating the methods and parameters used to create photogrammetric data products from RPAS-acquired imagery. Italicized words represent software settings used during data processing and model generation. Data were processed using Agisoft Metashape software (version 1.7.3).

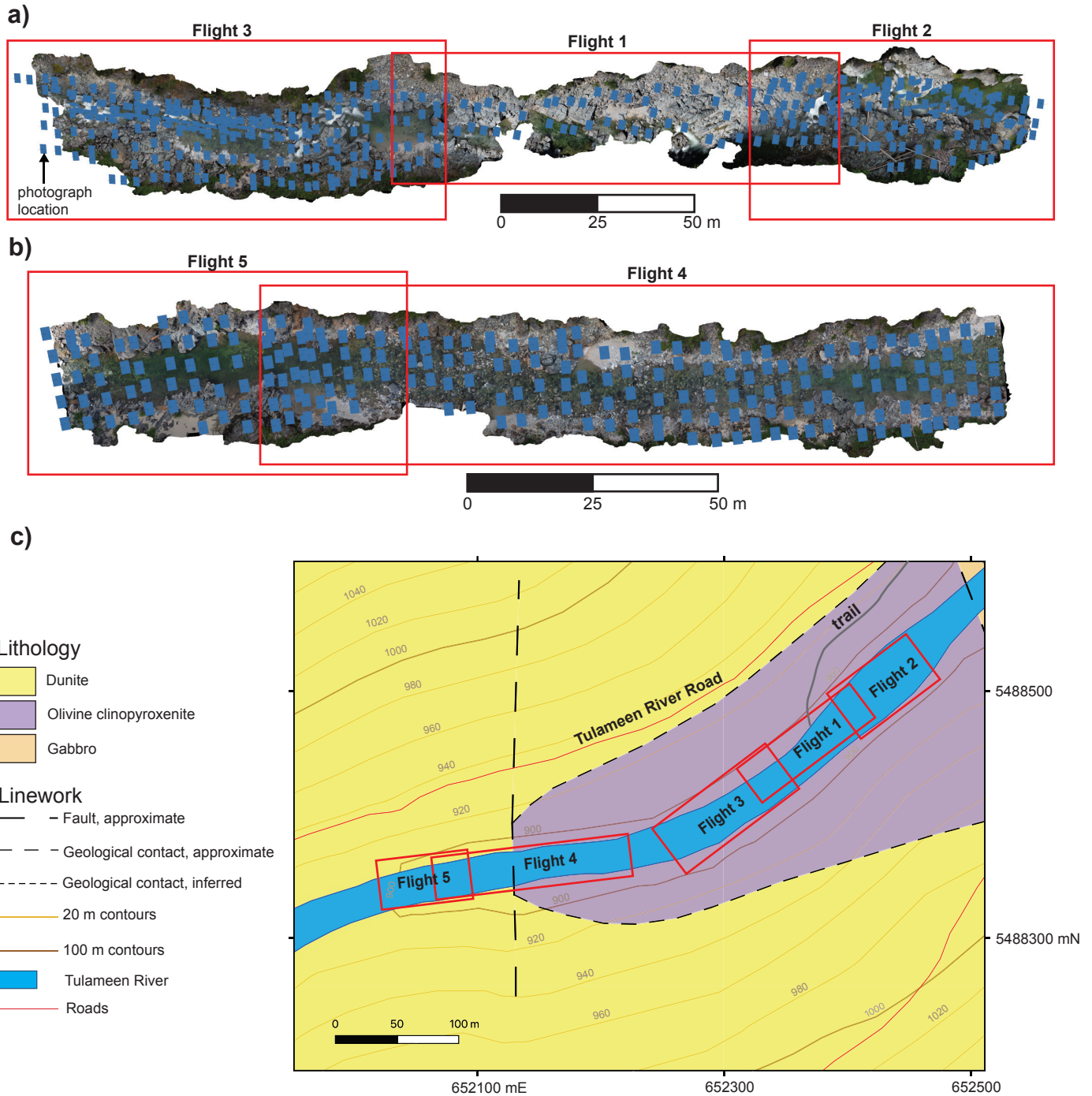


Fig. 6. RPAS survey flight and image locations. **a)** Photograph locations (blue squares) for flights 1, 2, 3. **b)** Photograph locations (blue squares) for flights 4 and 5. **c)** Locations of each flight (outlined by red boxes) on a simplified geological map centred on the Tulameen River (UTM Zone 10N, NAD83). Geology modified from (Nixon, 2018).

Table 1. Data acquisition and processing times for flights 1, 2, and 3, and 4 and 5.

Combined area	Photos	Combined flight time (min)	Sparse point cloud generation (min)	Dense point cloud generation (min)	Model generation (min)	DEM generation (min)	Orthomosaic Generation (min)	Total time (hrs)	File Size (GB)
Flights 1, 2, and 3	430	75	14.35	49.02	12.67	0.35	10.72	2.7	6.17
Flights 4 and 5	223	50	6.95	18.07	9.3	0.17	6.3	1.5	3.55

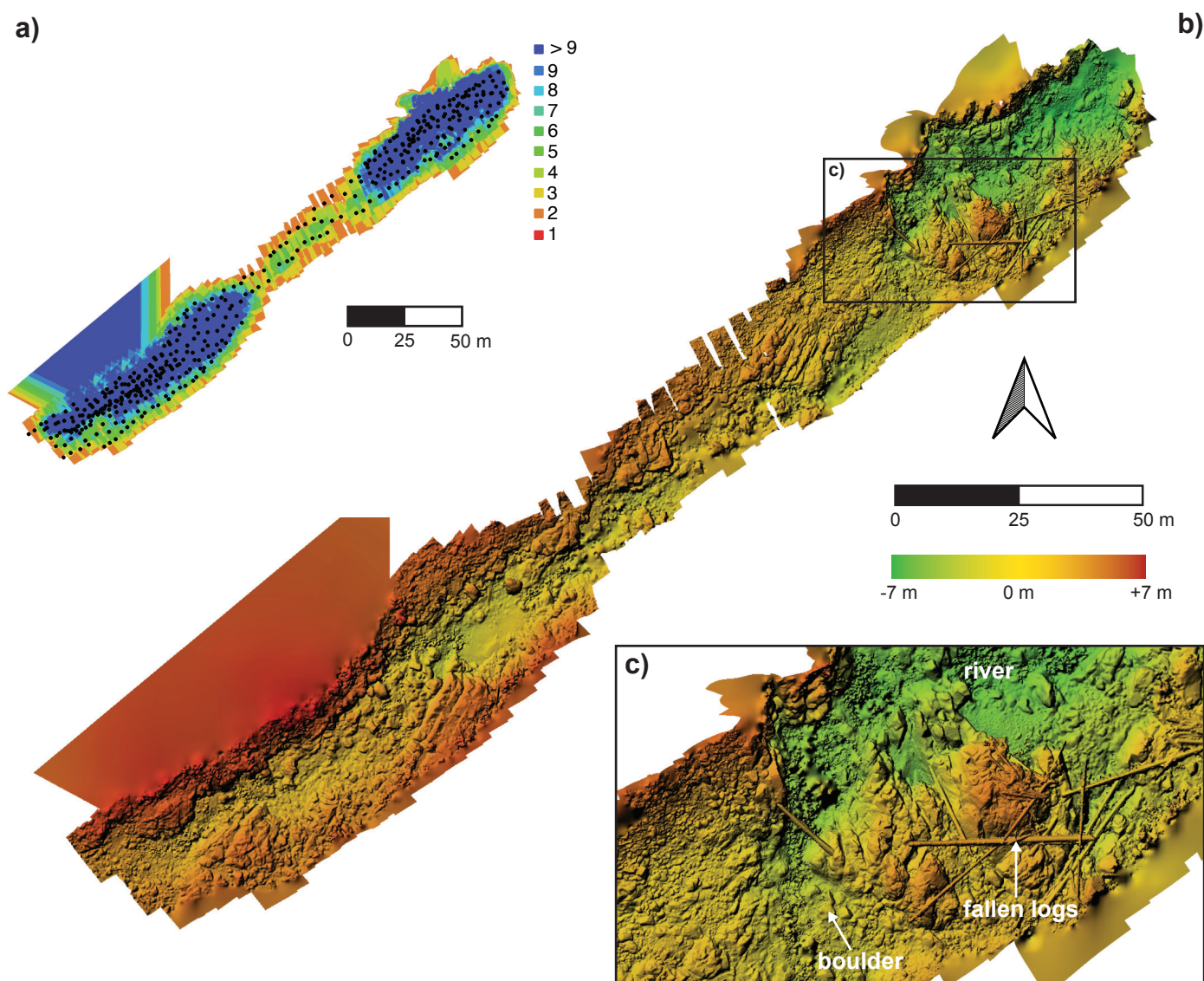


Fig. 7. Photograph density and digital elevation models along the Tulameen River section. **a)** Photograph density model of flights 1, 2, and 3. Black points indicate photograph-centres with each colour representing the number of overlapping photographs used in producing the DEM. **b)** Colourized photogrammetric DEM (resolution: 2.79 cm/pixel) of the river section covered by flights 1, 2, and 3. **c)** Detailed view of DEM showing bedrock topography, individual boulders, and fallen logs.

detail provided by the low-flying survey helps identify features in three-dimensions that would be unresolvable with existing elevation data. Features including individual boulders, fallen logs, and the river extent can be visualized in the DEM (Fig. 7c). Flight 2 traversed a cliff wall above the Tulameen River that is inaccessible by foot. To produce the digital model for this cliff, the RPAS was used to take overlapping photos at increasingly oblique angles to the vertical wall. The camera angle was flown at nadir and then decreased in 30-degree intervals accompanied by an approximately 3 m drop in elevation with each pass along the wall. This method enabled image alignment with the rest of the study area, and a greater level of detail to be recorded along the cliff.

Stitched imagery was overlain on the DEM to produce a georeferenced and coloured orthomosaic (Fig. 8a). The

orthomosaic sits in the olivine clinopyroxenite map unit of Nixon (2018) and spatially aligns with the satellite imagery, within a few m. Because of high colour contrast, the orthomosaic captures the detailed heterogeneity of rock types and their interrelationships in this generalized map unit. For example, a dunite body in clinopyroxenite (Fig. 8b), and olivine wehrlite and dunite in olivine clinopyroxenite are cut by layered and brecciated gabbro-diorite (Fig. 8c; see section 6). For the cliff surveyed in flight 2, close-up views of the model illustrate dunite dikes cutting olivine clinopyroxenite, both of which are cut by mafic dikes (Fig. 9).

6. Geology of the Tulameen River section

Low water levels of the Tulameen River in the summer of 2021 allowed us to examine a >4 km-long transect of

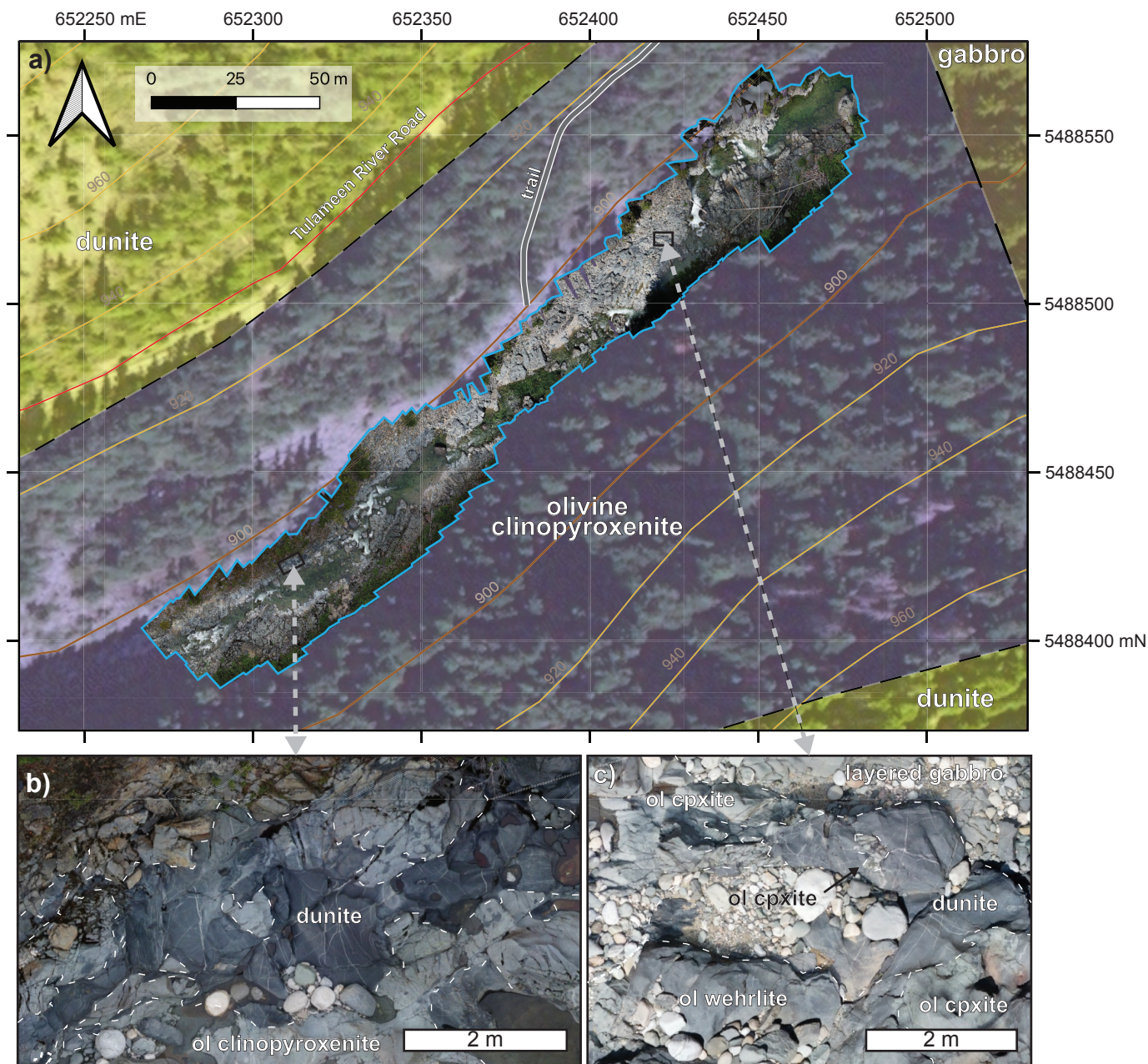


Fig. 8. Orthomosaic of the Tulameen River section covered by flights 1, 2, and 3. **a)** Complete stitched orthomosaic (outlined in blue) of flights 1, 2, and 3 overlain on Microsoft Bing composite satellite imagery (downloaded November 7, 2021) and a simplified geological map (modified from Nixon, 2018); see Fig. 6 for complete legend. **b)** and **c)** show detailed extracts from the orthomosaic. Abbreviations: ol = olivine; cpxite = clinopyroxenite.

continuous outcrop spanning the entire width of the northern portion of the Tulameen intrusion, from its western and eastern contacts with the Nicola Group. Contacts between the intrusion and Nicola Group country rocks are generally shear zones, although enclaves of Nicola Group enclosed by intrusive rocks were described by Nixon et al. (1997). From this transect, a detailed photogrammetric orthophoto (~270 m long) of outcrops along the Tulameen River (flights 1, 2, and 3) was annotated with features defined from both RPAS imagery and mapping on the ground (Fig. 10). The main rock type is clinopyroxenite. Dunite enclaves are present throughout the

area but tend to be more concentrated near larger bodies of dunite and wehrlite. Commonly, dunite enclaves are in clusters that are distributed along a westward trend. Some zones have rare dunite enclaves but have higher concentrations of dunite dikes. Layered gabbro-diorite dikes with cores of gabbro-diorite enclaves crosscut olivine clinopyroxenite and dunitic units. Fine-grained mafic to intermediate dikes occur in both the ultramafic rocks and the gabbroic intrusions. Carbonate alteration veins are spatially related to a prominent steeply dipping, north-striking shear zone.

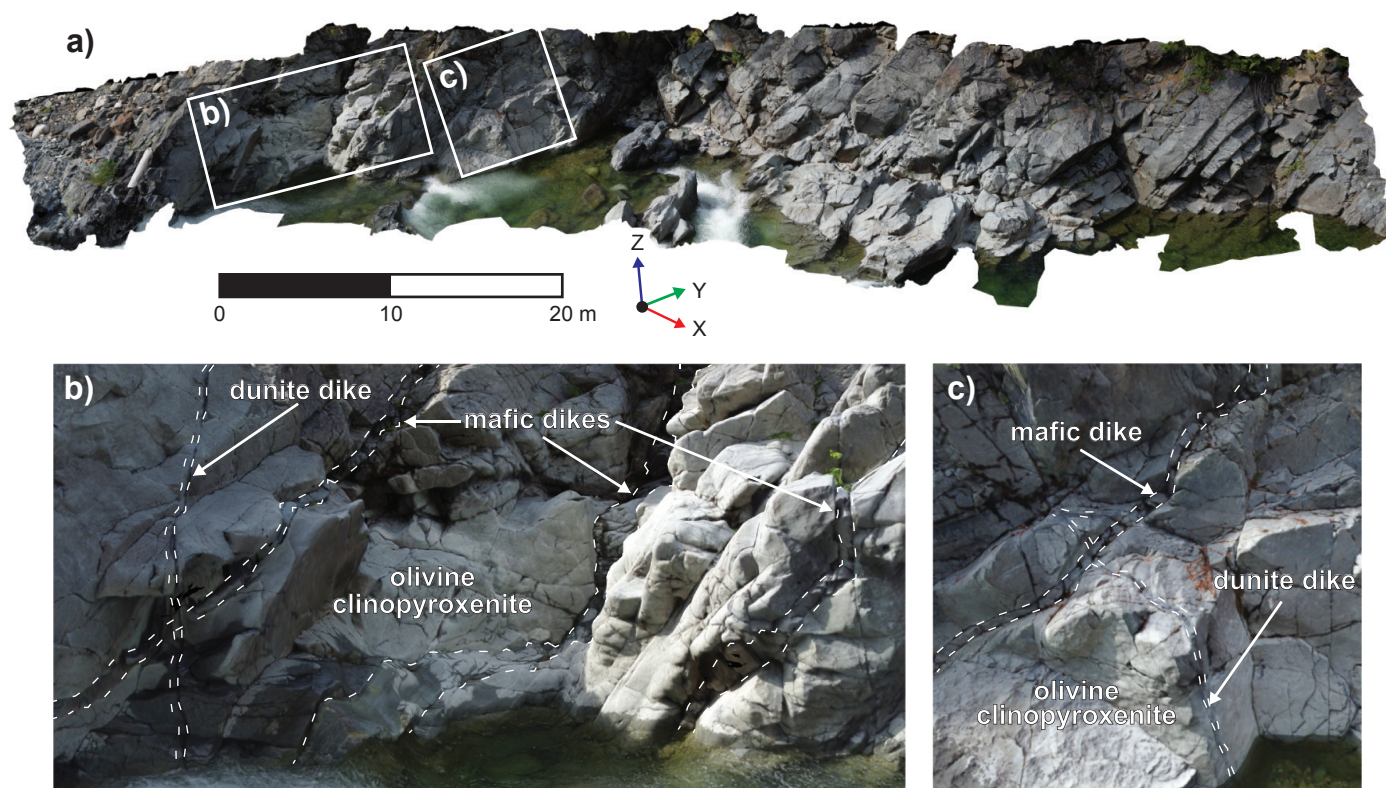


Fig. 9. Oblique 3D photogrammetric model along the Tulameen River created from RPAS-acquired photographs. **a)** Oblique 3D photogrammetric model of a cliff-face (flight 2). **b)** and **c)** are detailed extracts from the 3D model.

6.1. Lithological units

The Tulameen River section exposes many of the rock types in the Tulameen intrusion regionally, including dunite, olivine clinopyroxenite and clinopyroxenite, hornblende clinopyroxenite, gabbro and layered gabbro, and mafic to intermediate dikes (Fig. 11). Narrow (<10 m) north-trending shear zones commonly obscure primary intrusive contacts, and strain partitioning is common, with relatively incompetent rock types being more highly deformed. Primary intrusive relationships are locally preserved (Fig. 12).

6.1.1. Dunite

Regionally, dunite forms the core of the Tulameen intrusion in its northwestern part (Fig. 3). Dunite weathers orange-brown and has smooth to hackly-jointed surfaces caused by serpentinization fabrics. On fresh surfaces, dunite is generally dark grey (Fig. 11a) and, rarely, light green. This colouration is controlled by the degree of alteration. Dunite consists of >90 vol.%, fine-grained (<2 mm across) olivine (Fig. 2) and generally minor (<5 vol.%) interstitial accessory minerals. Although rare, dunite can also contain coarse-grained (>2 mm across) olivine in a matrix of smaller olivine grains. Accessory minerals include interstitial clinopyroxene and fine-grained, subhedral to euhedral chromite. Trace biotite may also be present. The dunite locally contains discontinuous segregations of chromite (Fig. 11a, inset) and massive chromitite layers and schlieren. The size and morphology of chromitite in the dunite core ranges from small mm-scale nodules to m-long

layers. Chromitite layers and segregations are deformed and discontinuous, providing evidence for remobilization of cumulates. Chromitites in the Tulameen intrusion may enclose grains of platinum group minerals (Cabri et al., 1973; St. Louis et al., 1986; Nixon et al., 1997) such as Pt-Fe alloys, tulameenite (Pt_2CuFe), and sperrylite (PtAs_2).

Dunite forms a discrete unit and also forms cm- to m-scale enclaves and discrete bodies in olivine clinopyroxenite (Figs. 8b, 13, 14). The olivine clinopyroxenite unit east of the dunite core (Fig. 10) preserves dunite enclaves of different sizes and shapes (Fig. 13). The enclaves commonly have sharp and cusped-lobate contacts with their olivine clinopyroxenite host and are typically amoeboid in shape. Where isolated, enclaves may be rounded (Fig. 13b), but they commonly terminate with sharp tips (Fig. 13d). The dunite is homogeneous, except for coarse to pegmatitic clinopyroxene and segregations containing clots (>5 mm diameter) of clinopyroxene (Figs. 14a-c). Clusters of small dunite enclaves are also near larger, 10-20 m-wide bodies of dunite and wehrlite. These clusters commonly form elongate zones that have an approximate easterly trend (Fig. 13a) and may have an interconnected system of dunite stringers (Fig. 13c). Dunite and olivine wehrlite locally have diffuse contacts with wehrlite, which, in turn, has diffuse contacts with olivine clinopyroxenite (Figs. 8c, 13d). The shapes of enclaves and diffuse contacts suggest mechanical disaggregation of poorly consolidated and ductile cumulates before final crystallization.

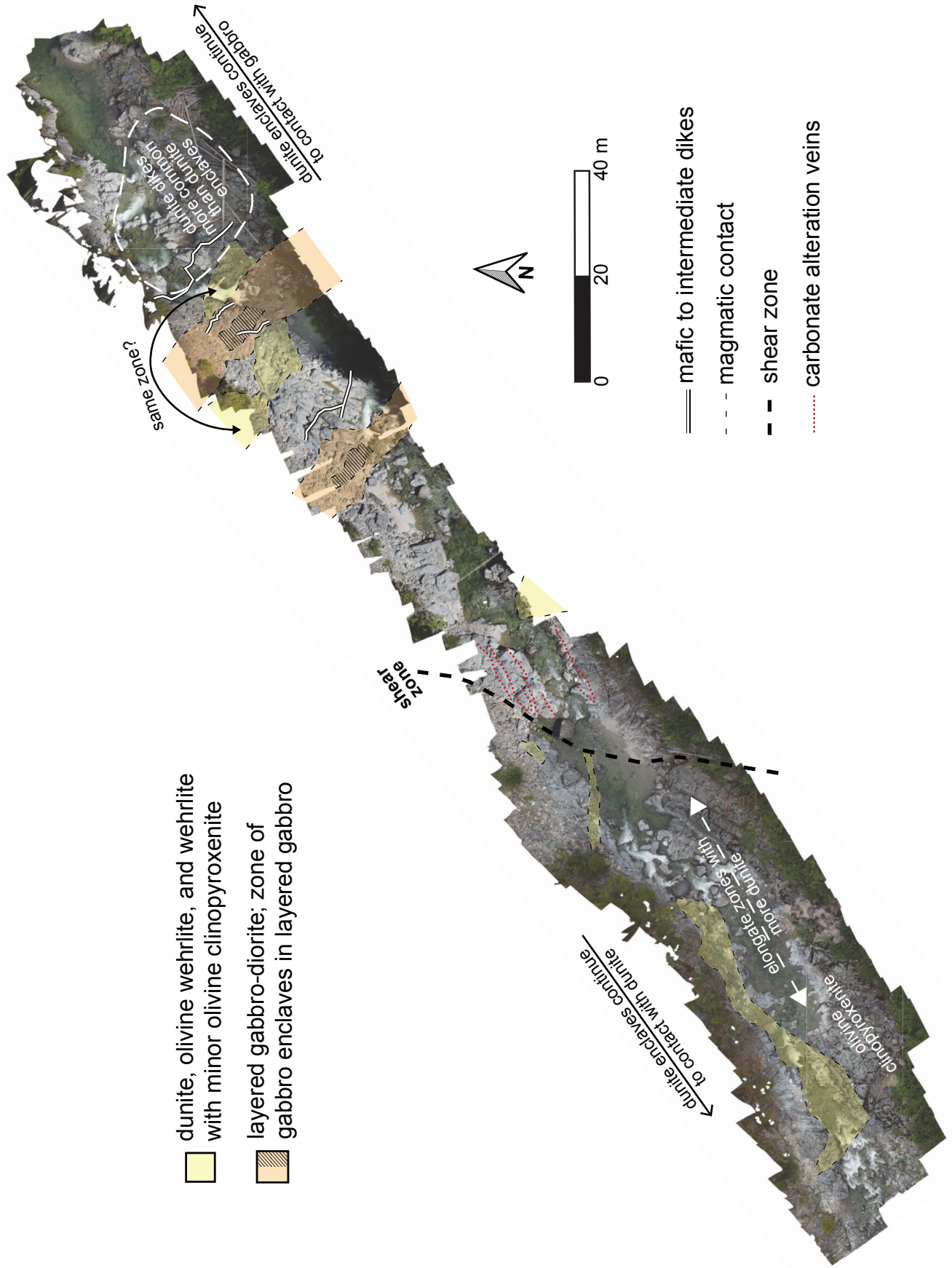


Fig. 10. Photogrammetric orthophoto of outcrops along the Tulameen River (flights 1, 2, and 3) annotated with intrusive, structural, and alteration trends defined from both RPAS imagery and mapping on the ground.

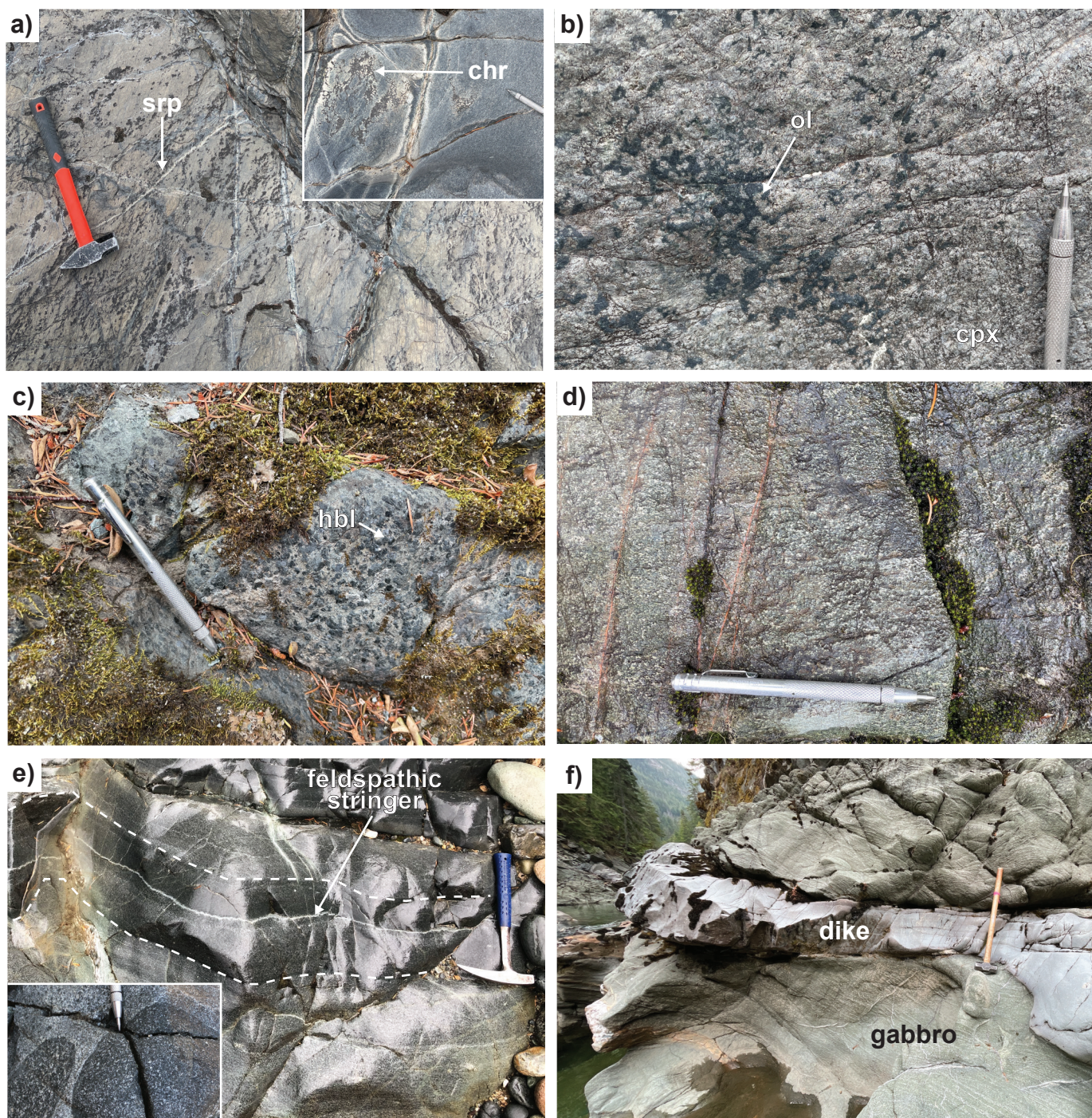


Fig. 11. Representative intrusive rock types in the Tulameen River transect. **a)** Dun-brown dunite with serpentine veins and chromite schlieren (inset). **b)** Close-up of olivine clinopyroxenite showing heterogeneously distributed dark olivine grains in a matrix of grey clinopyroxene. **c)** Hornblende clinopyroxenite with spotty, black hornblende crystals in a grey-green matrix of clinopyroxene. **d)** Gabbro with typical grey-and-white speckled appearance; the green tint is due to saussuritization of plagioclase. **e)** Layering in ca. 10 m-wide tabular gabbro bodies. Inset illustrates rounded gabbroic enclaves in the central portions of these tabular bodies. **f)** Fine-grained mafic to intermediate dike, cutting gabbro. Abbreviations: srp = serpentine; chr = chromite; ol = olivine; cpx = clinopyroxene; hbl = hornblende.

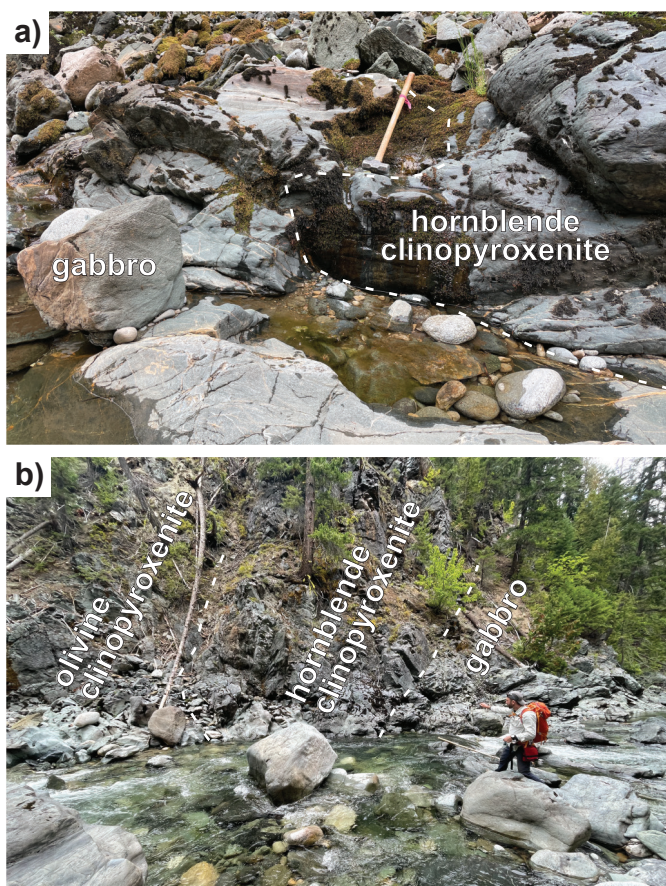


Fig. 12. Representative examples of intrusive contacts in the Tulameen intrusion. **a)** Sharp intrusive contact of gabbro cutting hornblende clinopyroxenite. **b)** Intrusive contacts between gabbro, hornblende clinopyroxenite, and olivine clinopyroxenite.

Dunite dikes are common in zones of intermingled cumulates in olivine clinopyroxenite (Figs. 9b, c, 15). The dikes are <10 cm wide, have sharp contacts, and display pinch and swell, pinch-out, bend, and bifurcation geometries rather than simple tabular bodies. Dunite dikes commonly crosscut deformed and disaggregated dunite and wehrlite enclaves (Figs. 15b-c). Small dike-like dunite projections extend from some dunite enclaves (Fig. 15d).

6.1.2. Olivine clinopyroxenite and clinopyroxenite

Regionally, olivine clinopyroxenite (Fig. 11b) and clinopyroxenite are on the margins of the dunite core and form discrete northwest-trending bodies (Fig. 3). Olivine clinopyroxenite and clinopyroxenite weather light grey-green and, where polished by the Tulameen River, have a mottled black appearance due to serpentinized olivine. Olivine clinopyroxenite contains 10-40 vol.% olivine and 60-90 vol.% clinopyroxene, whereas clinopyroxenite has >90 vol.% clinopyroxene and <10 vol.% olivine (Fig. 2). Clinopyroxene grains are typically 2-5 mm in diameter, but locally may be as large as 8 cm. Clinopyroxenite locally contains discontinuous layers of magnetite and may include trace biotite. Defining units

of olivine clinopyroxenite by modal abundance is challenging in the Tulameen intrusion because olivine is commonly present in clumps or segregations (Fig. 11b) rather than dispersed homogeneously throughout the rock.

Clinopyroxenite rarely forms distinct units within the dunite core, occurring as discontinuous segregations of homogeneous clinopyroxenite up to 1 m-wide (Fig. 16a) and as thin (<10 cm) dikes (Figs. 16b, c). Clinopyroxenite dikes are continuous over 100s of m; they are undulatory and may pinch-out (Fig. 16b) or be broken into discrete segments (Fig. 16c). These characteristics are inferred to indicate that interstitial liquids from an olivine-rich cumulate were expelled to form semi-tabular bodies. The break-up of tabular clinopyroxenite dikes fails to preserve crosscutting relationships within the dunite, suggesting that the clinopyroxenite formed in a hot, variably mobile body of dunite that experienced post-intrusion deformation before final solidification.

Rarely, clinopyroxenite and magnetite define igneous layering in the olivine clinopyroxenite unit (Fig. 17a). Centimetre- to dm-scale tabular units of dunite, wehrlite, and olivine clinopyroxenite with diffuse boundaries also define igneous layering (Fig. 17b). Locally, zones of magnetite-bearing olivine clinopyroxenite form lenses in clinopyroxenite. These lenses contain an internal fabric defined by alignment of olivine-rich zones in a matrix of apparently undeformed clinopyroxene crystals (Fig. 18), features that are consistent with syn-magmatic strain.

6.1.3. Hornblende clinopyroxenite

Regionally, hornblende clinopyroxenite (Fig. 11c) is mainly on the margins of the Tulameen intrusion, extending along its length (Fig. 3). It is volumetrically minor in the Tulameen River section relative to dunite, olivine clinopyroxenite, and gabbro. Black crystals of hornblende in grey-green weathering clinopyroxenite give the hornblende clinopyroxenite a distinctive spotted appearance. Although the hornblende grain size averages 2-10 mm, it is locally pegmatitic. Where grain size is large, coarse biotite is common. Rarely, hornblende clinopyroxenite contains segregations with an increased modal abundance of interstitial plagioclase, locally grading into gabbro.

The contacts between hornblende clinopyroxenite and crosscutting gabbro may be sharp (Fig. 12a), gradational (Fig. 12b), or brecciated with fragments of hornblende clinopyroxenite in a gabbro matrix and hornblende clinopyroxenite containing stringers of gabbro.

6.1.4. Gabbro and layered gabbro

Gabbro to syenogabbro extends along the eastern portion of the Tulameen intrusion, thinning toward the northwest (Fig. 3). In the Tulameen River section, gabbro is green-grey and white speckled due to plagioclase feldspar (Fig. 11d); the proportion of mafic minerals relative to plagioclase varies and is locally foliated. The main constituents (plagioclase, clinopyroxene, hornblende) have a limited grain size variation (2-4 mm

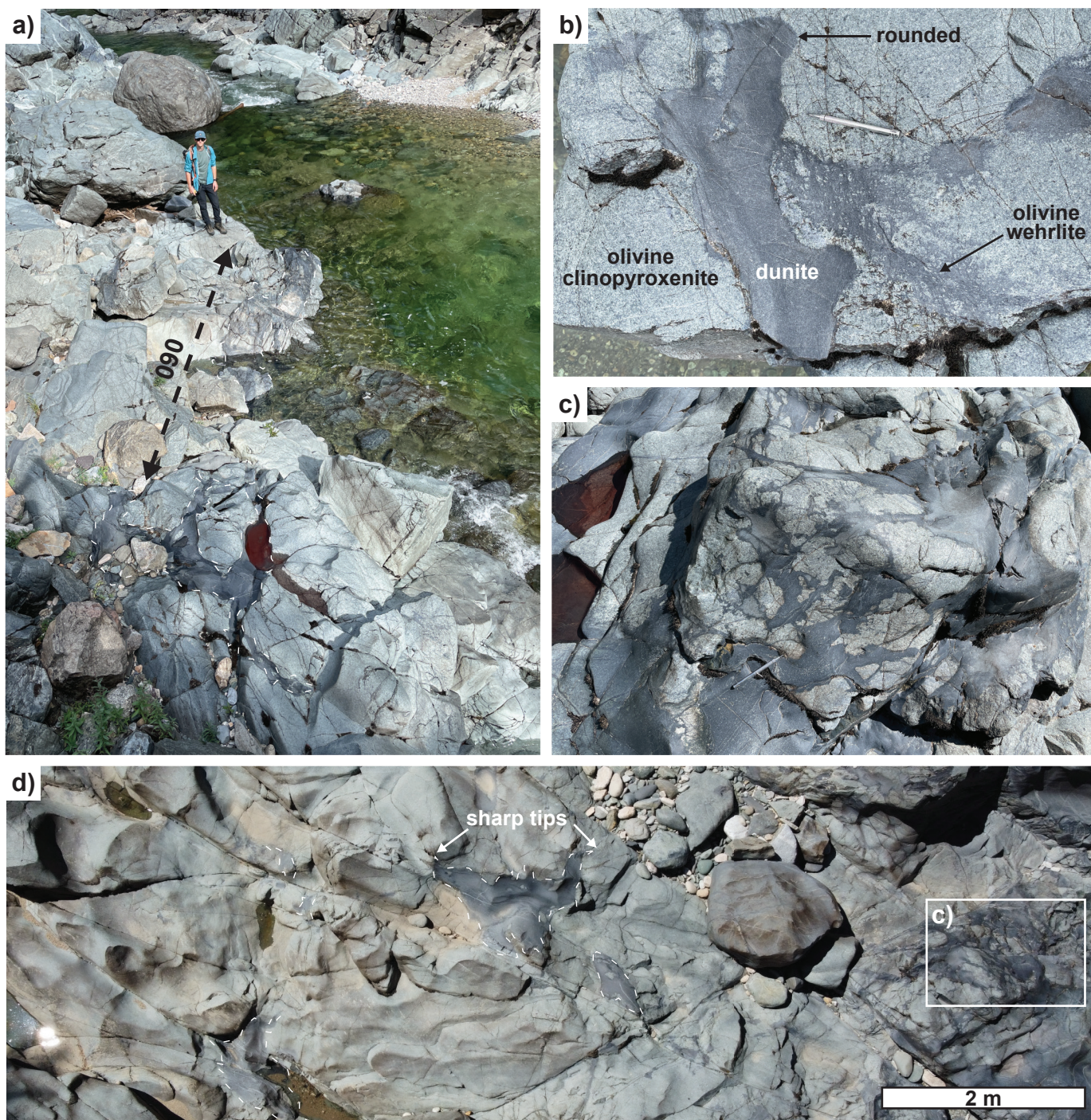


Fig. 13. Representative examples of dunite enclaves and clusters (dark rock) in olivine clinopyroxenite (light rock). **a)** Stringy, elongate dunite enclaves, many of which trend east. **b)** Ameboid blob of dunite in olivine clinopyroxenite, disaggregated dunite, and olivine wehrlite. **c)** Dunite (dark) forming an interconnected network in olivine clinopyroxenite with minimal crystal-scale disaggregation. See box in d) for location. **d)** Photograph from RPAS illustrating isolated dark dunite enclaves in olivine clinopyroxenite. Dunite enclaves commonly have sharp, undulatory contacts with olivine clinopyroxenite and sharp tips.

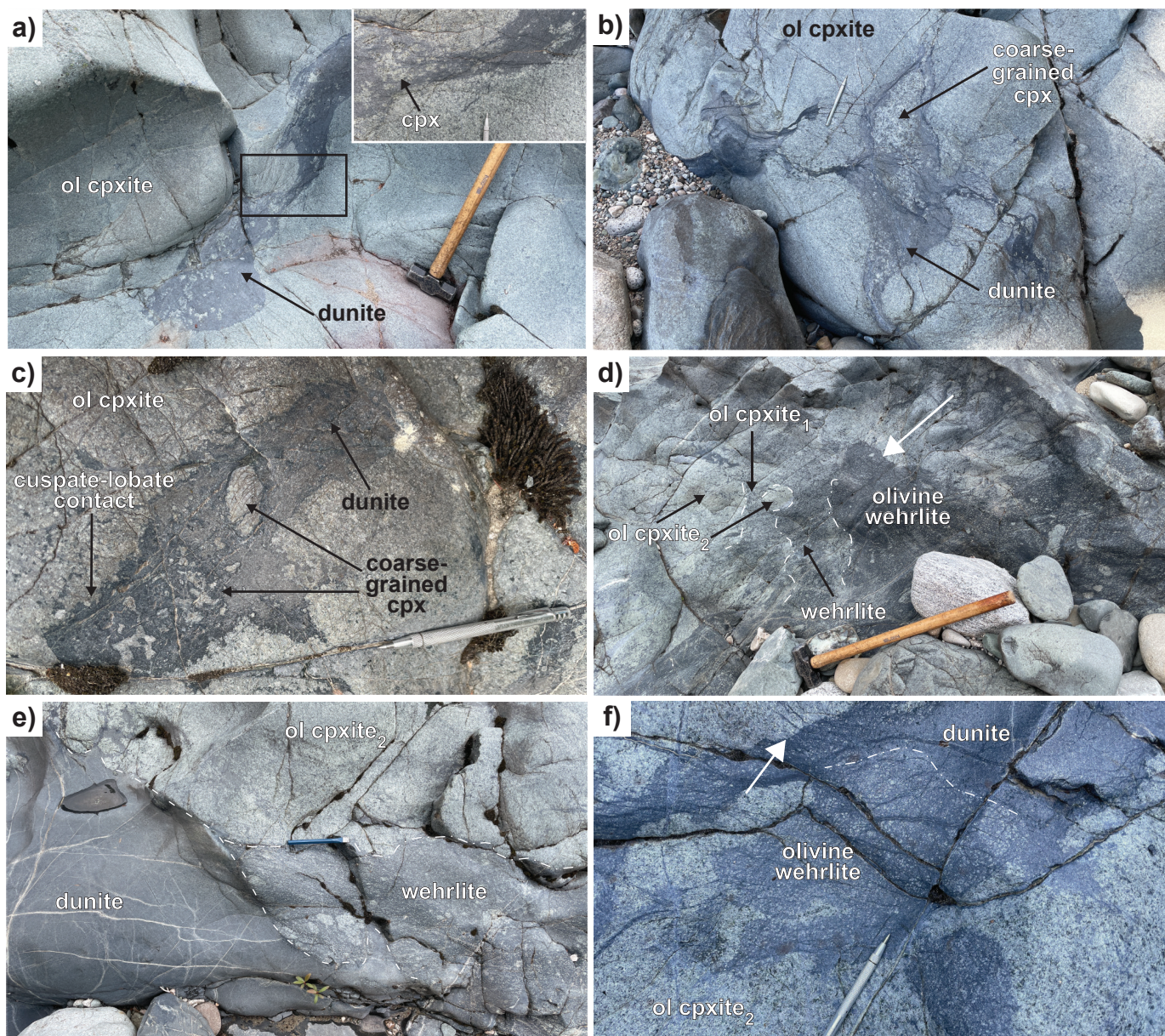


Fig. 14. Dunite enclaves with diverse morphological and textural relationships. a-c) Morphologies of dunite enclaves with coarse-grained to pegmatitic clinopyroxenite. **a)** Dunite enclave with ca. 4 cm-wide clinopyroxene crystals (inset) in medium-grained olivine clinopyroxenite. **b)** Dunite enclave with coarse segregation of olivine clinopyroxenite. **c)** Dunite enclave with cusped-lobate, locally flame-like contact against olivine clinopyroxenite; elliptical and amoeboid bodies of coarse-grained clinopyroxene inside the dunite enclave. d-f) Examples of diffuse contacts (dot-dash white lines) between olivine wehrlite or dunite and olivine clinopyroxenite. **d)** Gradational contact between olivine wehrlite and olivine clinopyroxenite, between wehrlite and olivine clinopyroxenite with >20 vol.% olivine (“ol cpxite₁”), and between olivine clinopyroxenite with >20 vol.% olivine and olivine clinopyroxenite with <20 vol.% olivine (“ol cpxite₂”). Olivine wehrlite also shows a sharp contact (dashed white line) with a rounded enclave of ol cpxite₂ and diffuse contact with ol cpxite₂ (white arrow). **e)** Diffuse contact between wehrlite and olivine clinopyroxenite, and sharp contact with (cross-cutting?) dunite. **f)** Dunite enclave with a diffuse contact against olivine wehrlite; olivine wehrlite with a diffuse contact against olivine clinopyroxenite. The top of the dunite enclave has a sharp contact with olivine clinopyroxenite (white arrow). Abbreviations: cpx = clinopyroxene; cpxite = clinopyroxenite; ol = olivine.

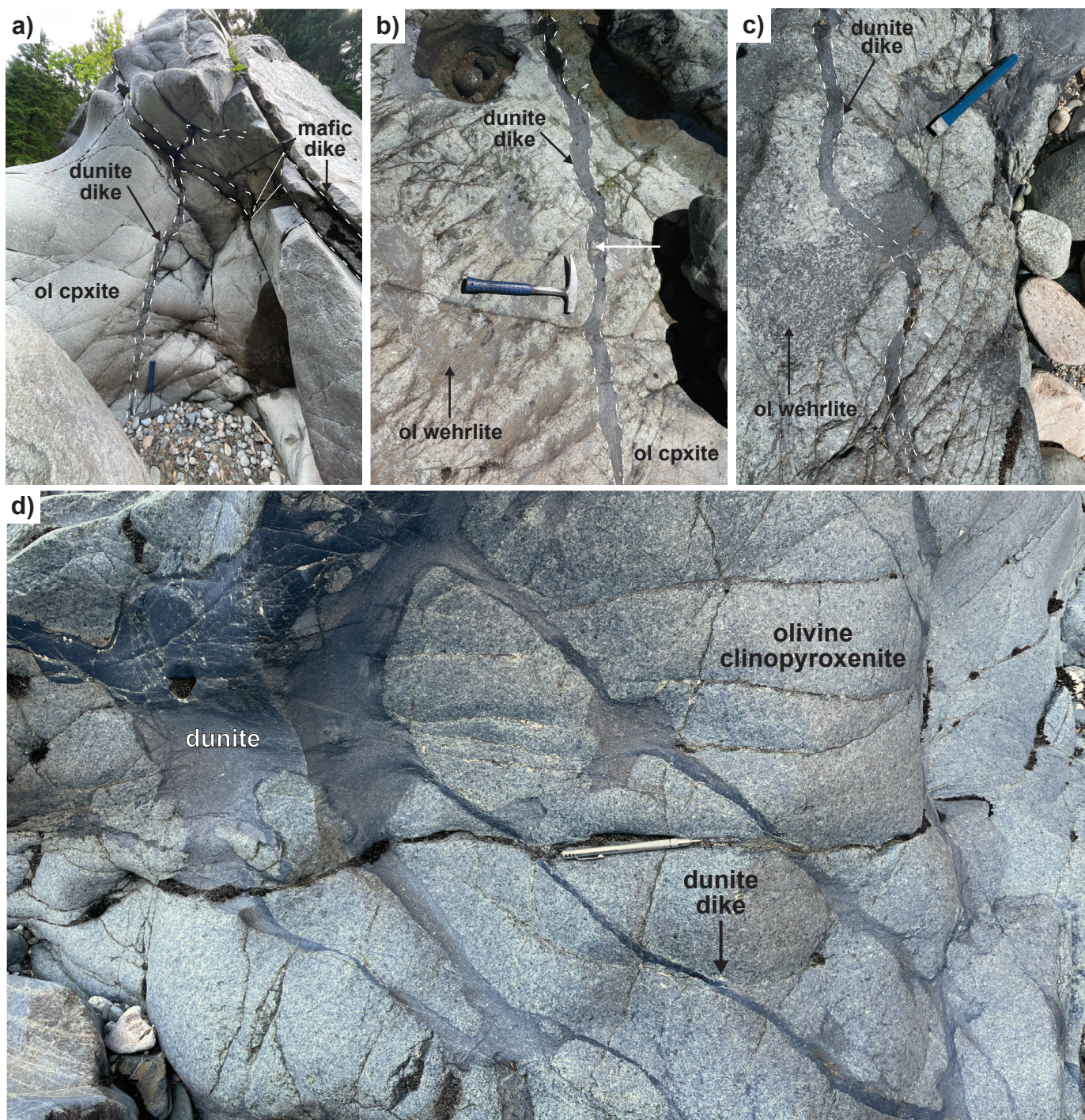


Fig. 15. Dunite dikes in olivine clinopyroxenite. **a)** Discontinuous and undulatory ca. 5 cm-wide dunite dike; the dike is subvertical and trends east-west. The dunite dike is crosscut by a ca. 10 cm-wide mafic dike that has either been offset or pinches out. **b)** A 5-7 cm-wide, undulatory dunite dike with small enclaves of olivine clinopyroxenite (white arrow). This dike crosscuts olivine clinopyroxenite with olivine wehrlite enclaves. The dunite dike has a general strike and dip of 045/45°SE. **c)** A ca. 2 cm-wide dunite dike crosscutting olivine clinopyroxenite with disaggregated dunite. The dike is undulatory, subvertical, and strikes east-west. **d)** Dunite dikes emanating from a dunite enclave. Abbreviations: cpxite = clinopyroxenite; ol = olivine.

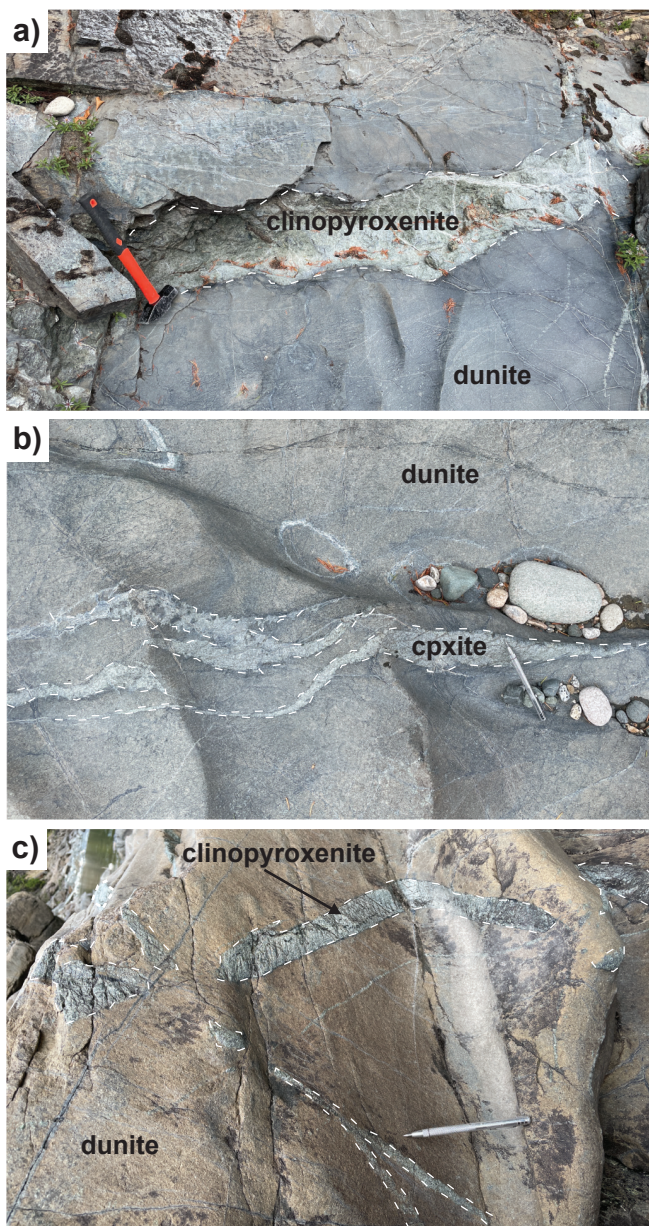


Fig. 16. Clinopyroxenite cutting dunite. **a)** Body of clinopyroxenite in dunite with sharp, undulatory contacts. **b)** Thin (1 to >5 cm-wide) clinopyroxenite dikes with sharp contacts and cusped-lobate margins in dunite. **c)** Tabular, discontinuous clinopyroxenite dikes with sharp contacts in dunite. Abbreviations: cpxite = clinopyroxenite.

diameter). The green colouration of gabbro results from intense saussuritization of plagioclase.

Late intrusions exposed in the Tulameen River include layered gabbro-diorite tabular bodies (Figs. 10, 11e) and fine-grained mafic to intermediate dikes (Figs. 10, 11f). The layered gabbro-diorite forms two tabular bodies that dip steeply southwest and cut olivine clinopyroxenite. These bodies are approximately 10 m-wide and contain upper and lower zones bounding an interior zone containing gabbro-diorite enclaves. Layering is defined by variations in relative proportions of hornblende and plagioclase. The layers are locally graded, with the amount



Fig. 17. Magmatic layering in ultramafic rocks. **a)** Interlayered clinopyroxenite and magnetite; layering also defined by grain size variation in clinopyroxenite. **b)** Boulder illustrating tabular units with diffuse boundaries of dunite (1), wehrlite (2), and olivine clinopyroxenite (3) considered to represent magmatic layering. Inset shows an irregular pegmatitic segregation with a dunite rim and coarse clinopyroxene core.



Fig. 18. Magnetite-bearing olivine clinopyroxenite lens and clinopyroxenite (white dashed lines). Olivine-rich zones are aligned to define a fabric, likely recording syn-magmatic strain.

of hornblende decreasing toward what was presumably the paleosurface, and basal erosional scours are common. The interior zones of these tabular bodies contain rounded to subangular blocks (<1 m) of leucocratic to melanocratic gabbro-diorite (Fig. 11e, inset). These blocks are in a matrix of gabbro-diorite with a different modal abundance of the same constituent minerals. Feldspathic stringers are both concordant and discordant with layering (Fig. 11e). Contacts with olivine clinopyroxenite are sharp and have chilled margins, suggesting that olivine clinopyroxenite had cooled before intrusion of the layered units.

6.1.5. Mafic to intermediate dikes

Fine-grained mafic to intermediate dikes, <3 m wide, are common in the Tulameen River section, and crosscut every rock type, except dunite (Figs. 10, 11f). These dikes are dark grey-green to pinkish grey and aphanitic to fine grained. Dikes are commonly tabular, with sharp contacts that may undulate in a general northwest trend. Bifurcations and abrupt jogs in the trend of the dikes are common. The widest dikes display dike-parallel layering and dike centers may have phenocrysts of pyroxene up to 2 mm in diameter. The mafic to intermediate dikes are commonly observed within shear zones and are also sub-parallel to igneous layering in the gabbro-diorite tabular bodies, suggesting that they were injected along pre-existing anisotropies. Locally, the dikes cut this layering. Nixon et al. (1997) considered these dikes as feeders for lavas in the Princeton Group (Eocene).

7. Discussion

7.1. Geologic fieldwork assisted by remotely piloted aircraft systems

Unlike traditional two-dimensional field photographs, the orientation of contacts and relationships between rock types can be documented in their entirety using an RPAS (e.g., Fig. 10). The models provide the ability to dynamically pan, zoom, and reorient observations at any scale and enable detailed 3D examination of inaccessible outcrops such as cliff faces by foot. The resultant digital models can also be used to digitally archive the physical conditions of a field site at point in time, such as the exceptional outcrop exposed due to low water levels along the Tulameen River in the summer of 2021. Generally, using RPAS can reduce time spent documenting outcrop-scale geological relationships, which are recorded in 3D and scaled by the photogrammetric model. Additionally, RPAS-assisted geological mapping provides real-time aerial perspectives for outcrop-scale mapping that are unattainable while on the ground, which may provide context for geological relationships. In this study, the use of RPAS and subsequent photogrammetric models decreased the duration of field work at the Tulameen River section, which allowed for detailed investigation elsewhere in the Tulameen intrusion.

7.2. Implications for Tulameen magmatic processes

In mafic plutonic systems, numerical modelling predicts

fluidization and mixing of resident crystal mush near sites of new magma injection (Bergantz et al., 2015; Schleicher et al., 2016). Preliminary observations from the present study, including remobilized and deformed chromitite layers and zones of intermingled and disaggregated olivine clinopyroxenite and dunite cumulates, are consistent with recharge and remobilization of crystal-rich magma mushes over a range of physical and rheological conditions in the ultramafic portions of the Tulameen intrusion. Similar observations and interpretations have been made from recent studies of the Polaris Alaskan-type intrusion (e.g., Nixon et al., 2020; Nott et al., 2020a, 2020b).

8. Conclusions

This study of the Tulameen Alaskan-type ultramafic-mafic intrusion of south-central British Columbia is an example of how RPAS-acquired photogrammetric models can aid geological mapping in areas of exceptional outcrop. RPAS photogrammetric surveys enable efficient archiving of 3D visual data, and allow observations of inaccessible geological features. The rock types exposed in the Tulameen River include dunite, olivine clinopyroxenite, hornblende clinopyroxenite, gabbro, layered gabbro-diorite, and mafic to intermediate dikes. Magma mingling relationships between dunite, wehrlite, and olivine clinopyroxenite are common and the textural diversity indicates a dynamic crystallization environment. Ongoing work will test geochemical predictions for the emplacement and mixing of crystal-rich magma mushes by characterizing major, minor, and trace element chemistry of the constituent minerals through both electron-probe microanalysis (EPMA) and laser ablation-inductively coupled plasma-mass spectrometry (LA-ICP-MS).

Acknowledgments

We thank Andrea Sanlorenzo for exceptional assistance and discussion while in the field and Travis Ferbey and Easton Elia for discussions regarding RPAS equipment and photogrammetric analysis. Thanks to Ken Hickey for general advice pertaining to field mapping. The senior author is grateful for salary assistance from an NSERC CGS-M scholarship. Funding for this project is provided by a NSERC Discovery Grant to James Scoates. This is a Natural Resources Canada Contribution #20210517. Constructive reviews of the manuscript by Alex Zagorevski, Travis Ferbey, and Lawrence Aspler are greatly appreciated.

References cited

- Annen, C., Blundy, J.D., Leuthold, J., and Sparks, R.S.J., 2015. Construction and evolution of igneous bodies: Towards an integrated perspective of crustal magmatism. *Lithos*, 230, 206-221.
- Balaguer-Puig, M., Marqués-Mateu, Á., Lerma, J.L., and Ibáñez-Asensio, S., 2017. Estimation of small-scale soil erosion in laboratory experiments with Structure from Motion photogrammetry. *Geomorphology*, 295, 285-296.
- Bergantz, G.W., Schleicher, J.M., and Burgisser, A., 2015. Open-system dynamics and mixing in magma mushes. *Nature Geoscience*, 8, 793-796.

- Cabri, L.J., Owens, D.R., and Laflamme, J.H.G., 1973. Tulameenite, a new platinum-iron-copper mineral from placers in the Tulameen River Area, British Columbia. *Canadian Mineralogist*, 12, 21-25.
- Camsell, C., 1913. Geology and mineral deposits of the Tulameen District, British Columbia. Geological Survey of Canada, Memoir 26, 188 p.
- Carrivick, J.L., Smith, M.W., Quincey, D.J., and Carver, S.J., 2013. Developments in budget remote sensing for the geosciences. *Geology Today*, 29, 138-143.
- Colpron, M., and Nelson, J.L., 2011. A digital atlas of terranes for the Northern Cordillera. British Columbia Ministry of Energy and Mines, British Columbia Geological Survey Geofile, 2011-11.
- Elia, E., and Ferbey, T., 2020. Generating photogrammetric DEMs in the field from remotely piloted aircraft systems. In: *Geological Fieldwork 2019*, British Columbia Ministry of Energy, Mines and Petroleum Resources, British Columbia Geological Survey Paper 2020-1, pp. 189-200.
- Eltner, A., Kaiser, A., Castillo, C., Rock, G., Neugirg, F., and Abellán, A., 2016. Image-based surface reconstruction in geomorphometry-merits, limits and developments. *Earth Surface Dynamics*, 4, 359-389. <<https://doi.org/10.5194/esurf-4-359-2016>>
- Findlay, D.C., 1963. Petrology of the Tulameen ultramafic complex, Yale District, British Columbia. Unpublished Ph.D. thesis, Queen's University, Kingston, Ontario, 415 p.
- Findlay, D.C., 1969. Origin of the Tulameen ultramafic-gabbro complex, southern British Columbia. *Canadian Journal of Earth Sciences*, 6, 399-425.
- Greig, C.J., Armstrong, R.L., Harakal, J.E., Runkle, D., and van der Heyden, P., 1992. Geochronometry of the Eagle Plutonic Complex and the Coquihalla area, southwestern British Columbia. *Canadian Journal of Earth Sciences*, 29, 812-829.
- Hansman, R.J., and Ring, U., 2019. Workflow: From photo-based 3-D reconstruction of remotely piloted aircraft images to a 3-D geological model. *Geosphere*, 15, 1393-1408. <<https://doi.org/10.1130/GES02031.1>>
- Himmelberg, G.R., and Loney, R.A., 1995. Characteristics and petrogenesis of Alaskan-type ultramafic-mafic intrusions, southeastern Alaska. U.S. Geological Survey Professional Paper, 1564, 47 p.
- Irvine, T.N., 1974. Petrology of the Duke Island ultramafic complex, southeastern Alaska. *Geological Society of America, Memoir* 138, 240 p.
- Jackson-Brown, S., 2017. Origin of the Cu-PGE-rich sulphide mineralization in the DJ/DB zone of the Turnagain Alaskan-type intrusion, British Columbia. Unpublished M.Sc. thesis, University of British Columbia, Vancouver, British Columbia, 290 p.
- James, M.R., and Robson, S., 2012. Straightforward reconstruction of 3D surfaces and topography with a camera: Accuracy and geoscience application. *Journal of Geophysical Research: Earth Surface*, 117, 17 p. <<https://doi.org/10.1029/2011JF002289>>
- James, M.R., Chandler, J.H., Eltner, A., Fraser, C., Miller, P.E., Mills, J.P., Noble, T., Robson, S., and Lane, S.N., 2019. Guidelines on the use of structure-from-motion photogrammetry in geomorphic research: *Earth Surface Processes and Landforms*, 44, 2081-2084.
- Kemp, J.F., 1902. The geological relations and distribution of platinum and associated metals. In: *Bulletin of the United States Geological Survey, Department of the Interior*, No. 193, 94 p.
- Le Maitre, R.W., 1989. A classification of igneous rocks and glossary of terms. Oxford, Blackwell Scientific Publications, 193 p.
- Logan, J.M., and Mihalynuk, M.G., 2014. Tectonic controls on early Mesozoic paired alkaline porphyry deposit belts (Cu-Au \pm Ag-Pt-Mo) within the Canadian Cordillera. *Economic Geology*, 109, 827-858.
- Manor, M.J., Wall, C.J., Nixon, G.T., Scoates, J.S., Pinsent, R.H., and Ames, D.E., 2014. Preliminary geology and geochemistry of the Giant Mascot ultramafic-mafic intrusion, Hope, southwestern British Columbia. British Columbia Ministry of Energy and Mines, British Columbia Geological Survey Open File 2014-3, 1:10,000 scale.
- Manor, M.J., Scoates, J.S., Nixon, G.T., and Ames, D.E., 2016. The Giant Mascot Ni-Cu-PGE deposit, British Columbia: mineralized conduits in a convergent margin tectonic setting. *Economic Geology*, 111, 57-87.
- Manor, M.J., Scoates, J.S., Wall, C.J., Nixon, G.T., Friedman, R.M., Amini, M., and Ames, D.E., 2017. Age of the Late Cretaceous ultramafic-hosted Giant Mascot Ni-Cu-PGE deposit, southern Canadian Cordillera: integrating CA-ID-TIMS and LA-ICP-MS U-Pb geochronology and trace element geochemistry of zircon. *Economic Geology*, 112, 1395-1418.
- Matzel, J.E., Bowring, S.A., and Miller, R.B., 2006. Time scales of pluton construction at differing crustal levels: Examples from the Mount Stuart and Tenpeak intrusions, North Cascades, Washington. *Geological Society of America Bulletin*, 118, 1412-1430.
- Mosbrucker, A.R., Major, J.J., Spicer, K.R., and Pitlick, J., 2017. Camera system considerations for geomorphic applications of SfM photogrammetry: camera system configuration to optimize SfM imagery. *Earth Surface Processes and Landforms*, 42, 969-986.
- Mungall, J.E., Kamo, S.L., and McQuade, S., 2016. U-Pb geochronology documents out-of-sequence emplacement of ultramafic layers in the Bushveld Igneous Complex of South Africa. *Nature Communications*, 7, 13385. <<https://doi.org/10.1038/ncomms13385>>
- Nixon, G.T., and Rublee, V.J., 1988. Alaskan-type ultramafic rocks in British Columbia: New concepts of the structure of the Tulameen Complex. In: *Geological Fieldwork 1987*, British Columbia Ministry of Energy, Mines and Petroleum Resources, Paper 1988-1, pp. 281-294.
- Nixon, G.T., Cabri, L.J., and Laflamme, J.H.G., 1990. Platinum-group-element mineralization in lode and placer deposits associated with the Tulameen Alaskan-type complex, British Columbia. *The Canadian Mineralogist*, 28, 503-535.
- Nixon, G.T., Hammack, J.L., Ash, C.H., Cabri, L.J., Case, G., Connelly, J.N., Heaman, L.M., Laflamme, J.H.G., Nuttall, C., Paterson, W.P.E., and Wong, R.H., 1997. Geology and platinum group element mineralization of Alaskan-type ultramafic-mafic complexes in British Columbia. British Columbia Ministry of Employment and Investment, British Columbia Geological Survey, Bulletin 93, 142 p.
- Nixon, G.T., Manor, M.J., Jackson-Brown, S., Scoates, J.S., and Ames, D.E., 2015. Magmatic Ni-Cu-PGE sulphide deposits at convergent margins. In: Ames, D.E., and M.G. Houlé, M.G., (Eds.), *Targeted Geoscience Initiative 4: Canadian Nickel-Copper-Platinum Group Elements-Chromium Ore Systems-Fertility, Pathfinders, New and Revised Models*, Geological Survey of Canada, Open File 7856, pp. 17-34.
- Nixon, G.T., Scheel, J.E., Friedman, R.M., Wall, C.J., Gabites, J., Miller, D., and Scoates, J.S., 2017. Geology and geochronology of the Turnagain ultramafic-mafic intrusion, British Columbia. British Columbia Ministry of Energy, Mines and Petroleum Resources, British Columbia Geological Survey Geoscience Map 2017-1, 1:10,000 scale.
- Nixon, G.T., 2018. Geology of the Tulameen Alaskan-type ultramafic-mafic intrusion, British Columbia. British Columbia Ministry of Energy, Mines and Petroleum Resources, British Columbia Geological Survey Open File 2018-2, 1:20,000 scale.
- Nixon, G.T., Scoates, J.S., Milidragovic, D., Nott, J., Moerhuis, N., Ver Hoeve, T.J., Manor, M.J., and Kjarsgaard, I.M., 2020. Convergent margin Ni-Cu-PGE-Cr ore systems. In: *Targeted Geoscience Initiative 5: Advances in the Understanding of Canadian Ni-Cu-PGE and Cr Ore Systems*, Geological Survey of Canada Open File 8722, pp. 197-218.
- Nott, J., Milidragovic, D., Nixon, G.T., and Scoates, J.S., 2020a. New geological investigations of the Early Jurassic Polaris ultramafic-

- mafic Alaskan-type intrusion, north-central British Columbia. In: Geological Fieldwork 2019. British Columbia Ministry of Energy, Mines and Petroleum Resources, British Columbia Geological Survey, Paper 2020-1, pp. 59-76.
- Nott, J.A., Milidragovic, D., Nixon, G.T., and Scoates, J.S., 2020b. Geology of the Polaris Alaskan-type ultramafic-mafic intrusion, north-central British Columbia. British Columbia Ministry of Energy, Mines and Low Carbon Innovation, British Columbia Geological Survey Open File 2020-4, 1:15,000 scale.
- Paterson, S.R., 2009. Magmatic tubes, pipes, troughs, diapirs, and plumes: Late-stage convective instabilities resulting in compositional diversity and permeable networks in crystal-rich magmas of the Tuolumne batholith, Sierra Nevada, California. *Geosphere*, 5, 496-527. <<https://doi.org/10.1130/GES00214.1>>
- Rice, H.M.A., 1947. Geology and mineral deposits of Princeton map area, British Columbia. Geological Survey of Canada, Memoir 243, 136 p.
- Rublee, V.J., 1989. The structural control of the Tulameen complex and outlying ultramafic bodies, 92H/7, 10. In: Exploration in British Columbia 1988. British Columbia Ministry of Energy, Mines and Petroleum Resources, British Columbia Geological Survey, pp. B71-B81.
- Rublee, V.J., 1994. Chemical petrology, mineralogy and structure of the Tulameen complex, Princeton area, British Columbia. Unpublished M.Sc. thesis, University of Ottawa, Ottawa, Ontario, 183 p.
- Scheel, J.E., 2007. Age and origin of the Turnagain Alaskan-type intrusion and associated Ni-sulphide mineralization, north-central British Columbia, Canada. Unpublished M.Sc. thesis, University of British Columbia, Vancouver, British Columbia, 210 p.
- Scheel, J.E., Scoates, J.S., and Nixon, G.T., 2009. Chromian spinel in the Turnagain Alaskan-type ultramafic intrusion, northern British Columbia, Canada. *The Canadian Mineralogist*, 47, 63-80.
- Schleicher, J.M., Bergantz, G.W., Breidenthal, R.E., and Burgisser, A., 2016. Time scales of crystal mixing in magma mushes. *Geophysical Research Letters*, 43, 1543-1550.
- Schoene, B., Schaltegger, U., Brack, P., Latkoczy, C., Stracke, A., and Guenther, D., 2012. Rates of magma differentiation and emplacement in a ballooning pluton recorded by U-Pb TIMS-TEA, Adamello Batholith, Italy. *Earth and Planetary Science Letters*, 355-356, 162-173.
- Scoates, J.S., Wall, C.J., Friedman, R.M., Weis, D., Mathez, E.A., and VanTongeren, J.A., 2021. Dating the Bushveld Complex: Timing of crystallization, duration of magmatism, and cooling of the world's largest layered intrusion and related rocks. *Journal of Petrology*, 62, 1-39.
- Shervais, K., 2016. Structure from Motion (SfM) Photogrammetry Field Methods Manual for Students. Unpublished Manual, University NAVSTAR Consortium (UNAVCO), National Science Foundation and NASA, 10 p.
- Smith, M.W., Carrivick, J.L., and Quincey, D.J., 2016. Structure from motion photogrammetry in physical geography. *Progress in Physical Geography: Earth and Environment*, 40, 247-275.
- Spence, D.W., 2020. Olivine in the Polaris Alaskan-type intrusion of north-central British Columbia: Implications for the magmatic evolution of primitive arc magmas and for convergent margin Ni-Cu-PGE ore-forming systems. Unpublished B.Sc. thesis, University of British Columbia, Vancouver, British Columbia, 144 p.
- St. Louis, R.M., Nesbitt, B.E., and Morton, R.D., 1986. Geochemistry of platinum group elements in the Tulameen ultramafic complex, southern British Columbia. *Economic Geology*, 81, 961-973.
- Transport Canada, 2021. Canadian Aviation Regulations (SOR/96-433), 1001 p.
- Wall, C.J., Scoates, J.S., Weis, D., Friedman, R.M., Amini, M., and Meurer, W.P., 2018. The Stillwater Complex: integrating zircon geochronological and geochemical constraints on the age, emplacement history and crystallization of a large, open-system layered intrusion. *Journal of Petrology*, 59, 153-190.
- Weinberg, R.F., Vernon, R.H., and Schmeling, H., 2021. Processes in mushes and their role in the differentiation of granitic rocks. *Earth-Science Reviews*, 220, 1-30.
- Westoby, M.J., Brasington, J., Glasser, N.F., Hambrey, M.J., and Reynolds, J.M., 2012. 'Structure-from-Motion' photogrammetry: A low-cost, effective tool for geoscience applications. *Geomorphology*, 179, 300-314.
- Yao, Z., Mungall, J.E., and Jenkins, M.C., 2021. The Rustenburg Layered Suite formed as a stack of mush with transient magma chambers. *Nature Communications*, 12, 505. <<https://10.1038/s41467-020-20778-w>>